



**HAL**  
open science

## **An adjoint approach for the analysis of RANS closure using pressure measurements on a high-rise building**

Mohamed Yacine Ben Ali, Gilles Tissot, Dominique Heitz, Sylvain Aguinaga,  
Etienne Mémin

► **To cite this version:**

Mohamed Yacine Ben Ali, Gilles Tissot, Dominique Heitz, Sylvain Aguinaga, Etienne Mémin. An adjoint approach for the analysis of RANS closure using pressure measurements on a high-rise building. 2020. hal-03076369v1

**HAL Id: hal-03076369**

**<https://hal.science/hal-03076369v1>**

Preprint submitted on 16 Dec 2020 (v1), last revised 9 Mar 2022 (v2)

**HAL** is a multi-disciplinary open access archive for the deposit and dissemination of scientific research documents, whether they are published or not. The documents may come from teaching and research institutions in France or abroad, or from public or private research centers.

L'archive ouverte pluridisciplinaire **HAL**, est destinée au dépôt et à la diffusion de documents scientifiques de niveau recherche, publiés ou non, émanant des établissements d'enseignement et de recherche français ou étrangers, des laboratoires publics ou privés.

Banner appropriate to article type will appear here in typeset article

# 1 **An adjoint approach for the analysis of RANS** 2 **closure using pressure measurements on a high-rise** 3 **building**

4 **M.Y. Ben Ali<sup>1,2</sup>†, G. Tissot<sup>2</sup>, D. Heitz<sup>3</sup>, S. Aguinaga<sup>1</sup> and E. Mémin<sup>2</sup>**

5 <sup>1</sup>Centre Scientifique et Technique du Bâtiment (CSTB), 11 rue Henri Picherit, F-44300 Nantes, France

6 <sup>2</sup>INRIA, Fluminance team, Campus universitaire de Beaulieu, F-35042 Rennes, France

7 <sup>3</sup>INRAE, UR OPAALE, F-35044 Rennes Cedex, France

8 (Received xx; revised xx; accepted xx)

9 In this study we investigate the closure of a common turbulence model for Reynolds averaged  
10 Navier-Stokes (RANS) in the framework of variational data assimilation prediction of wind  
11 flows around big structures. This study considers practical experimental settings where only  
12 sparse wall-pressure data, measured in a wind tunnel, are available. The evaluation of a cost  
13 functional gradient is efficiently carried out with the exact continuous adjoint of the RANS  
14 model. Particular attention is given to the derivation of the adjoint turbulence model and the  
15 adjoint wall law. Given the dual description of the dynamics, composed of the RANS model  
16 and its adjoint, some methodological settings that enable diagnosis of the turbulence closure  
17 are explored here. They range from adjoint maps analysis to global constants calibration and  
18 finally consider the adjunction of a distributed parameter. Numerical results on a high-rise  
19 building reveal a high reconstruction ability of the adjoint method. A good agreement in wind  
20 load and wake extension was obtained. As with sparse observations, the sensitivity field is  
21 generally not very regular for distributed parameters, a projection onto a space of more regular  
22 functions belonging to the Sobolev space ( $H^1$ ) is also proposed to strengthen the efficiency  
23 of the method. This has been shown to lead to a very efficient data assimilation procedure  
24 as it provides an efficient descent direction as well as a useful regularisation mechanism.  
25 Beyond providing an efficient data-driven reconstruction technique, the proposed adjoint  
26 methodology enables an in-depth analysis of the turbulence closure and finally improves it  
27 significantly.

28 **Key words:**

---

29 **MSC Codes** (*Optional*) Please enter your MSC Codes here

† Email address for correspondence: mohamed-yacine.ben-ali@inria.fr

**Abstract must not spill onto p.2**

## 30 1. Introduction

31 During their lifetime, buildings are continuously exposed to wind coming from all directions.  
32 Particularly, due to their extended exposed surface, high-rise buildings and big structures  
33 undergo extremely strong lateral aerodynamic forces. As a consequence, large lateral  
34 deflections or, even more, some problematic tearing affecting security may be observed.  
35 Yet, by having a prior understanding of the airflow surrounding these big structures, wind  
36 loads can be predicted and such issues avoided. To understand how these turbulent flows  
37 affect the structures, physical models along with numerical simulations are usually deployed.  
38 On the one hand, for more than a century, experiments with scaled models of buildings  
39 have been carried out in wind tunnels (Cermak & Koloseus 1954; Jensen 1958). After  
40 years of advancement on measurement techniques together with an increased knowledge on  
41 wind dynamics, tunnel experiments have proven their reliability for loads prediction issues  
42 (Surry 1999; Cochran & Derickson 2011). High-Frequency Force Balance method (HFFB)  
43 (Tschanz & Davenport 1983) and High-Frequency Pressure Integration (HFPI) (Irwin &  
44 Kochanski 1995) are two examples of techniques employed for such effort measurements.  
45 Despite many improvements brought to deal with turbulent flows, such techniques provide  
46 only partial information of the complex wind-structure interactions involved. For instance,  
47 when the structure has a complex geometrical shape, the very sparse nature of the cladding  
48 pressure measurements brought by HFPI techniques may lead to a misrepresentation of the  
49 local pressure field.

50 On the other hand, more recently, thanks to the significant progress of computational  
51 capabilities, computational fluid dynamics (CFD) techniques have proved their value to give  
52 a complete representation of these flows, enabling a better understanding of the relation  
53 between the flow structures and the wind loads. However, since an accurate description  
54 of such turbulent flows requires a fine enough resolution, this technique may rapidly  
55 become impractical due to the large computational resources required. To go beyond this  
56 computational limitation, turbulence model closures associated with the Reynolds averaged  
57 Navier-Stokes (RANS) simulation were widely adopted to give an insight into the time-  
58 averaged flow profile. With such models, turbulence characteristics can be reasonably  
59 represented at lower computational costs. Over the years, motivated by the available  
60 computational wind engineering guidelines (Tominaga *et al.* 2008; EN 2005), several  
61 established turbulence models have been deeply investigated (Cochran & Derickson 2011;  
62 Meroney & Derickson 2014). While RANS simulations offer good qualitative results that are  
63 physically relevant, due to their inherent assumptions built from accumulated knowledge on  
64 real turbulent flows, close inspection on wind loads reveals typical failures in their prediction.  
65 For instance, early studies by Murakami (1990, 1997) compared the standard  $k - \epsilon$  model  
66 (Launder & Sharma 1974) analysis with unsteady large-eddy simulations (LES) and wind  
67 tunnel experiments. They revealed the model's poor accuracy resulting in an over-production  
68 of turbulent kinetic energy in the flow impingement region. Various revisions of the model  
69 (*e.g.*, RNG by Yakhot *et al.* (1992), realizable by Shih *et al.* (1995), MMK by Tsuchiya *et al.*  
70 (1997)) have provided results close to measures obtained in wind tunnels. Yet, recent studies  
71 have shown that such models still fail to reproduce an accurate recirculation region behind  
72 the building (Tominaga & Stathopoulos 2010, 2017; Yoshie *et al.* 2007).  
73 This accuracy issue may strongly hinder the model predictive skill when compared to  
74 real-world measurements. One way to correct this deficiency consists in devising methods  
75 allowing to couple turbulence modelling with measurements.

76 Indeed, during the last decades, a wide variety of coupling techniques has been increasingly  
77 considered in fluid mechanics applications. Such techniques, commonly termed as data  
78 assimilation (DA), have been employed to estimate an optimal flow state provided by a

79 given dynamical model such that it remains close enough to observations. So far, two  
80 different classes of DA techniques have been applied to that end. On the one hand, Bayesian  
81 techniques, often referred to as sequential DA techniques, have been used to estimate optimal  
82 flow parameters from data affected by a high uncertainty level (Meldi & Poux 2017; Mons  
83 *et al.* 2016). On the other hand, optimal control techniques, like variational DA or ensemble-  
84 variational DA, have been proposed for direct and large eddy numerical description models  
85 (Mons *et al.* 2016; Gronskis *et al.* 2013; Yang *et al.* 2015; Mons *et al.* 2017; Li *et al.* 2020;  
86 Chandramouli *et al.* 2020). In this latter kind of approaches, DA is formulated as a constrained  
87 optimisation problem (Bryson 1975). A cost functional, reflecting the discrepancies between  
88 some (incomplete) measurements of the flow variables and a numerical representation of the  
89 flow dynamics, is minimised using a gradient-based descent method. In such an optimisation  
90 problem, the functional gradient's evaluation is efficiently carried out through the dynamical  
91 model's adjoint instead of a costly finite difference approach (Errico 1997; Plessix 2006). At  
92 this point, these DA methods were often used to reconstruct initial conditions and/or boundary  
93 conditions for nonstationary flow simulation issues (such as large eddy simulations). In the  
94 last few years, mean flow reconstruction problems have also been considered with data  
95 assimilation techniques. In some studies (Foures *et al.* 2014; Symon *et al.* 2017), built from  
96 variational DA techniques, the authors considered laminar steady Navier-Stokes equations  
97 corrected by an unknown volume-force to directly model the turbulence effects. These  
98 studies showed that, in laminar or transitional flows, such models perform well to assimilate  
99 synthetic particle image velocimetry (PIV) data. Other DA studies at high Reynolds number  
100 were performed with RANS turbulence models (Li *et al.* 2017; Singh & Duraisamy 2016;  
101 Franceschini *et al.* 2020). In these works, mean flow DA approaches exploited the turbulence  
102 models' structure, which results from a trade-off between asymptotic theories on turbulence  
103 mixing and empirical tuning to fit experimental data. This was expressed through a calibration  
104 process of the closure constants or of a corrective source term added to the turbulence model.  
105 Experimental knowledge plays here a crucial role. Such studies dealt mainly with fundamental  
106 and industrial oriented flow configurations in which turbulence is often generated at a  
107 unique integral scale. However, to the authors' knowledge, for flow configurations involving  
108 complex flow interactions as in the case of an atmospheric boundary layer around a bluff-  
109 body, turbulence closure structure analysis using DA techniques are still largely unexplored.  
110 Nevertheless, it is noteworthy that formal uncertainty quantification (UQ) techniques have  
111 been employed to interpret these closure models in probabilistic terms (Etling *et al.* 1985;  
112 Duynkerke 1988; Tavoularis & Karnik 1989; Edeling *et al.* 2014; Margheri *et al.* 2014). For  
113 example, in a recent work by Shirzadi *et al.* (2017), global coefficients of the standard  $k - \epsilon$   
114 model were adapted for unstable atmospheric boundary layer (ABL) flow around high-rise  
115 buildings using a forward UQ technique (*e.g.*, Monte Carlo simulations).

116 In the present work, we propose investigating one of the most common turbulence closure  
117 models for RANS modelling in a variational data assimilation procedure framework. A  
118 continuous adjoint approach is considered and then discretised using a 3D finite volume  
119 scheme. Without loss of generality, we will, first, use this methodology to investigate the  
120 sensitivity fields of the global closure coefficients of the high Reynolds realizable revision  
121 of the  $k - \epsilon$  model (Shih *et al.* 1995). Their physical interpretation will enable us to  
122 point out limits on such closure models' applicability for data-model coupling purposes,  
123 particularly for wind flows around buildings. Contrary to previous data-model studies in  
124 which velocity measurements were considered on significant parts of the flow domain, we  
125 rely on sparse pressure data measured on the building surface. This difference is far from  
126 being cosmetic as it leads so far to a much more practical experimental setting for large-scale  
127 volumetric measurements. Besides, we point out some difficulties faced in the literature  
128 in coupling RANS modeled 3D flows with only parietal experimental measurements. This

129 framework will discuss limitations and improvements in estimating wind loads and mean  
 130 velocities surrounding a high-rise building. To address the limitations of common turbulence  
 131 modelling more efficiently, we will then relax the model rigidity by considering a distributed  
 132 additive control parameter in the turbulent dissipation transport equation, where the closure  
 133 is performed. Beyond the fact that it provides a better agreement with real flow data due  
 134 to the richer control parameter space and avoids overfitting to the data thanks to the  
 135 prior information brought by the RANS model structure, the optimal control parameter  
 136 enables us to identify features that are missing in the initial RANS closure hypotheses.  
 137 To that end, a modified dissipation rate equation and its adjoint equation are introduced.  
 138 A physical interpretation of the reconstructed field will then be addressed to point out the  
 139 limits of models' closure applicability for data-model coupling purposes. In the optimisation  
 140 procedure, the adjoint sensitivity field and the associated cost functional gradient is generally  
 141 irregular for distributed control parameters due to the lack of specific treatment. This lack  
 142 of regularity often even hinders a proper estimation of the sensitivity map and requires the  
 143 adjunction of regularisation terms whose calibration is not straightforward. In contrast to  
 144 this conventional approach, a projection onto a space of regular functions: the Sobolev space  
 145  $H^1(\Omega)$ , is proposed to regularise the descent direction. As will be shown, this leads to a very  
 146 efficient data assimilation procedure.

147 The paper is organised as follows. We first describe the adjoint-based turbulence model and  
 148 wall-pressure measurements coupling for flow reconstruction around a high-rise building.  
 149 The next section improves the adjoint-based turbulence models' sensitivity analysis tool and  
 150 proposes a corrective turbulence model. Then, the case studied is described. The models'  
 151 sensitivities are discussed, and their performances for flow reconstruction from wall-pressure  
 152 data are presented. Finally, a summary and further outlook are given.

## 153 2. Development for an adjoint-based diagnostics

154 In this section, we set up the variational data-model coupling framework, based on optimal  
 155 control techniques. A particular attention is given to the analytical derivation of the adjoint  
 156 model of one of the most common turbulence models, the realizable revision of  $k-\epsilon$ , coupled  
 157 with near wall closure.

### 158 2.1. Variational approach

159 A generic variational data-coupling problem can be formally described by the following  
 160 optimisation problem :

$$162 \quad \begin{aligned} & \min_{\alpha} \quad \mathcal{J}(\alpha, \mathbf{X}(\alpha), \mathbf{Y}_{\text{obs}}) \\ & \text{subject to} \quad M_i(\alpha, \mathbf{X}(\alpha)) = 0 \quad i = 1, \dots, N \end{aligned} \quad (2.1)$$

163 where  $\mathcal{J}()$  is the cost function that quantifies the misfit between observations and the model,  
 164 *i.e.* here measurements and CFD solution respectively, penalised by an *a priori* statistical  
 165 knowledge of these discrepancies in the form of a covariance matrix. Here we refer to the  
 166 flow measurements  $\mathbf{Y}_{\text{obs}}$ , and the predicted flow  $\mathbf{X}$ .  $N$  stands for the number of independent  
 167 variables necessary for a full description of the flow. The minimisation of this function is  
 168 constrained by the set of flow governing equations  $M_i$ . Such problem may be solved using  
 169 a gradient-based algorithm. It consists in iteratively evaluating the cost functional and its  
 170 sensitivity derivatives in order to find the minimum by successive updates of the control  
 171 variables  $\alpha$ . The sketch of the procedure is given in algorithm 1.

172 In order to properly define the cost function, one may proceed as follows. The only available  
 173 experimental inputs are wall-pressure measurements. Ideally, the discrepancy between the

---

**Algorithm 1**  $\min_{\alpha} \mathcal{J}(\alpha, \mathbf{X}(\alpha), \mathbf{Y}_{\text{obs}})$

---

**Initialisation:**  $\alpha^m = \alpha_b$  and  $m=0$

**repeat**

Solve  $\mathbf{M}(\mathbf{X}^m, \alpha^m) = 0$

Compute sensitivity  $\frac{D\mathcal{J}}{D\alpha}(\mathbf{X}^m, \alpha^m)$

update  $\alpha \rightarrow \alpha^{m+1}$  ;  $m = m + 1$

**until**  $\|\mathcal{J}^m - \mathcal{J}^{m-1}\| < \varepsilon$

---

174 experimental pressure measure and the model wall-pressure can be expressed as  $\Delta P^w =$   
 175  $P_{\text{obs}}^w - \mathcal{H}(P^w)$  where  $\mathcal{H}(\cdot)$  restricts the pressure at the measurement positions (the subscript  
 176  $w$  stands for wall). However, due to measurement errors, this difference must be weighted by  
 177 their associated uncertainties. Having no access to the real pressure values, these uncertainties  
 178 have to be estimated. By assuming a normal distribution around the measured value, this  
 179 can be introduced by means of an empirical covariance matrix. Concerning the projector  
 180  $\mathcal{H}(\cdot)$ , in this work, we have considered interpolation by a Gaussian kernel of half size  $D$ ,  
 181 i.e. the building diameter, from the computational grid to the position of the measurements  
 182 to ensure consistency between estimated observation and pressure measurements. So far, it  
 183 should be pointed out that under the assumption of incompressible flow, the pressure solved  
 184 numerically is only defined up to a constant. Thus, the experimental and numerical pressures  
 185 can best be collated by comparing their respective pressure coefficient  $C_p = \frac{P - P_{\infty}}{1/2\rho U_{\text{ref}}^2}$  with  
 186  $P_{\infty}$  denoting the reference static pressure. We note the difference between numerical and  
 187 experimental value by  $\Delta C_p = C_{p_{\text{obs}}}^w - C_p^w$ .

188 To ensure that the set of parameters  $\alpha$  remains in a realistic set of values, we define a  
 189 physically likely range for each component  $\alpha_i$ . This can be formalised by a penalisation term  
 190 on the cost functional, leading to

$$191 \quad \mathcal{J}(P, \alpha) = \left\| \frac{1}{2} \rho U_{\text{ref}}^2 \Delta C_p^w \right\|_{R^{-1}}^2 + \|\alpha - \alpha_b\|_B^2, \quad (2.2)$$

192 where  $R$  is the covariance matrix defined from measurement's uncertainties,  $B$  denotes the  
 193 covariance matrix associated to the parameter validity range, and  $U_{\text{ref}}$  stands for a reference  
 194 velocity. Without loss of generality, a diagonal measurement covariance with a constant  
 195 standard deviation  $\sqrt{\overline{R_{ii}}} = 1$  is used. This uniformity represents an equal degree of confidence  
 196 for each measurement, and the diagonal structure ensues from an assumption of spatially  
 197 uncorrelated errors, which can be assumed for sufficiently distant measurements. Matrix  $B$   
 198 corresponds to a *prior* knowledge on the range of values of the parameters. In practice, it  
 199 is worth noting that the role of  $B$  matrix is twofold. In the one hand, it imposes a realistic  
 200 interval in which the parameters can be optimised; while, on the other hand, it ensures a  
 201 consistent scaling between inhomogeneous terms.

## 202 2.2. A RANS model

203 The incompressible airflow surrounding the building can be fully described by its velocity  $\mathbf{u}$   
 204 and pressure  $p$ . This unsteady state, solution of the Navier-Stokes equations, can be further  
 205 decomposed in terms of its mean,  $(\mathbf{U}, P)$ , that will be resolved and a modeled fluctuation  
 206  $(\mathbf{u}', p')$ . By applying time averaging to the Navier-Stokes equations, one can obtain the partial  
 207 differential equations (PDEs) of the RANS equations in a conservative form, whose solution  
 208 provides the mean wind flow :

$$209 \quad \frac{\partial(\rho U_j U_i)}{\partial x_j} = -\frac{\partial P}{\partial x_i} + \mu \frac{\partial}{\partial x_j} \left[ \frac{\partial U_i}{\partial x_j} \right] - \frac{\partial}{\partial x_j} \left( \overline{\rho u'_i u'_j} \right), \quad (2.3)$$

$$210 \quad \frac{\partial U_j}{\partial x_j} = 0.$$

211 Due to the non-linear term, the averaging procedure leads to a second-order moment  $\overline{u'_i u'_j}$ ,  
 212 called the Reynolds stress. Since all the unsteadiness and turbulence effects of the wind  
 213 flow are contained in this term, without *a priori* specification of this term, the above system  
 214 is not closed and cannot be solved. The immediate solution for the closure is to include  
 215 additional transport equations to predict the turbulence second-order statistics. Relying on the  
 216 Boussinesq analogy between large-scale dissipation and molecular friction, Reynolds stresses  
 217 are commonly modeled using a turbulent diffusion-like term, so-called eddy viscosity model.  
 218 Several models have been proposed to relate quantities describing turbulent fluctuations. A  
 219 common practice associates the turbulent kinetic energy  $k$ , representing the isotropic part of  
 220 the exact Reynolds stress, with the turbulence length scale  $l$ . Due to their simple structures,  
 221 these models often require empirical closure functions or constants which are established and  
 222 determined from experimental knowledge, trying to ensure their widest possible applications.  
 223 For instance, the steady realizable  $k-\epsilon$  turbulence model (Shih *et al.* 1995), in which  $\epsilon \sim \frac{k^{3/2}}{l}$   
 224 models the turbulence dissipation rate at the viscous scale, is often adopted for wind flow  
 225 expertise around real-world buildings. The Reynolds stress is linearly linked to the mean  
 226 shear stress by an eddy viscosity as follows:

$$227 \quad -\overline{\rho u'_i u'_j} = \mu_t \left( \frac{\partial U_i}{\partial x_j} + \frac{\partial U_j}{\partial x_i} \right) - \frac{2}{3} \delta_{ij} \rho k, \quad (2.4)$$

228 where  $\mu_t$  stands for the isotropic (*i.e.* assuming that length and time scales of turbulence are  
 229 smaller than those of the mean flow with no preferential direction) eddy viscosity coefficient.  
 230 Its value is calculated using the relation

$$231 \quad \mu_t = C_\mu \rho \frac{k^2}{\epsilon}.$$

232 The coefficient  $C_\mu$ , following the work of Shih *et al.* (1995), is a non uniform constant defined  
 233 by

$$234 \quad C_\mu = \frac{1}{A_0 + A_s U_s \frac{k}{\epsilon}}, \quad (2.5)$$

235 where  $A_s$  and  $U_s$  are functions of the mean strain and rotation rates and  $A_0$  is a closure tuning  
 236 coefficient. Substituting the Reynolds stress model (2.4) in the mean momentum equation  
 237 (2.3) yields to

$$238 \quad \frac{\partial(\rho U_j U_i)}{\partial x_j} = -\frac{\partial}{\partial x_i} \left( P + \frac{2}{3} \rho k \right) + \frac{\partial}{\partial x_j} \left[ \mu_{eff} \left( \frac{\partial U_i}{\partial x_j} + \frac{\partial U_j}{\partial x_i} \right) \right], \quad (2.6)$$

239 where  $\mu_{eff} = (\mu_t + \mu)$  stands for an effective viscosity. It can be noted that the isotropic  
 240 component  $\frac{2}{3} \rho k$  is absorbed in a modified mean pressure and only the anisotropic part plays  
 241 an effective role in transporting momentum. It is worth noting that anisotropy here arises  
 242 only from the mean flow strain and does not depend on the turbulent fluctuations. Moreover,  
 243 in the computation of the pressure coefficient (required for the observation error in the cost  
 244 functional (2.2)), we subtract the isotropic part to obtain  $C_p = \frac{P - P_\infty - \frac{2}{3} \rho k}{1/2 \rho U_{ref}^2}$ . With regards to  
 245 the turbulence closure model, the transport of mean turbulent kinetic energy,  $k$ , is described  
 246 by

$$247 \quad \frac{\partial \rho U_j k}{\partial x_j} = \frac{\partial}{\partial x_j} \left[ \left( \mu + \frac{\mu_t}{\sigma_k} \right) \frac{\partial k}{\partial x_i} \right] + \mu_t \left( \frac{\partial U_i}{\partial x_j} + \frac{\partial U_j}{\partial x_i} \right) \frac{\partial U_i}{\partial x_j} - \rho \epsilon, \quad (2.7)$$

248 where  $\sigma_k$  is a closure constant that enables the scalar mixing of  $k$  to be affected by other  
 249 mechanisms than eddy viscosity. The hypothesis, associated to the value  $\sigma_k = 1$ , in which  
 250 the eddy diffusion affects in the same way the momentum and the turbulent kinetic energy  
 251  $k$ , is analysed in section 5.2.

252 The turbulent dissipation rate transport is described by the model proposed by Shih *et al.*  
 253 (1995)

$$254 \quad \frac{\partial \rho U_j \epsilon}{\partial x_j} = \frac{\partial}{\partial x_j} \left[ \left( \mu + \frac{\mu_t}{\sigma_\epsilon} \right) \frac{\partial \epsilon}{\partial x_i} \right] + C_1(S, k, \epsilon) S \epsilon - C_2 \frac{\epsilon^2}{k + \sqrt{\mu \epsilon}}, \quad (2.8)$$

255 where  $S = 2(S_{ij}S_{ij})^{\frac{1}{2}}$  is the magnitude of mean strain rate where  $S_{ij} = \frac{1}{2} \left( \frac{\partial U_i}{\partial x_j} + \frac{\partial U_j}{\partial x_i} \right)$  and  
 256  $C_1 = \max(0.43, \eta/(5 + \eta))$  where  $\eta = Sk/\epsilon$  is the normalised strain rate. The constants  $\sigma_\epsilon$   
 257 and  $C_2$  are closure coefficients that need to be calibrated. Assuming that the generation of  $\epsilon$   
 258 is linked to its redistribution everywhere, as it is was established in an inertial layer, leads to  
 259 a relationship between these coefficients (details in section 5.2.2). This closure hypothesis  
 260 is analysed as well in section 5.2. To properly close this set of equations (since the model is  
 261 valid only for high Reynolds regimes), an asymptotic behaviour has to be imposed near the  
 262 wall where this assumption is no longer valid in the viscous and buffer layers. Indeed, for  
 263 large scale configurations (*i.e.*, ABL, high-rise buildings), the first grid centre closest to the  
 264 wall usually falls at the high end of the logarithmic layer. Thus, with a finite volume scheme,  
 265 in the domain  $\Omega_c$ , covered by the first grid cell closest to the wall centered on  $|_c$  and with a  
 266 boundary face centered on  $|_f$  (see figure 1), these relations hold

$$267 \quad U^+|_c = \frac{1}{\kappa} f(y^+|_c), \quad (2.9)$$

$$268 \quad \frac{\partial k}{\partial x_j} n_j|_f = \frac{\partial \epsilon}{\partial x_j} n_j|_f = 0, \quad (2.10)$$

$$269 \quad P_k|_c = \epsilon|_c = \frac{u_\tau^2|_c}{\kappa y|_c} \quad (2.11)$$

$$270 \quad y^+|_c = \frac{\rho u_\tau|_c y|_c}{\mu}, \quad (2.12)$$

$$271 \quad \tau_{wall}|_c = \rho u_\tau^2|_c = \mu_{eff} \frac{U_i t_i|_c}{y|_c}, \quad (2.13)$$

$$272 \quad U^+|_c = \frac{U_i t_i|_c}{u_\tau|_c}, \quad (2.14)$$

274 where  $U^+$ ,  $y^+$  are the dimensionless wall unit tangential velocity component and distance  
 275 from wall, respectively,  $n_i$  and  $t_i = 1 - n_i$  are the projections of normal and tangential unit  
 276 vectors onto the boundary face in the orthonormal frame  $(x, y, z)$ . The log function  $f$  is an  
 277 empirical function parametrised by constants which depend on the wall type (such as smooth  
 278 or rough); and  $\kappa = 0.41$  is the Von Karman constant. As viscous effects is being neglected at  
 279 the center of the first cell where  $y^+ \gg O(1)$ , the friction velocity  $u_\tau$  is scaled by the square  
 280 root of the fluctuations, following the empirical expression  $u_\tau = C_\mu^{1/4} k^{1/2}$  with  $C_\mu = 0.09$ . Let  
 281 us note that (2.13) extends the constant shear stress to the wall as we assume linear behaviour  
 282 (in second order finite volume scheme FVM) inside the cell  $\Omega_c$ . In practice, this extension  
 283 is of great importance as it enables the enforcement of the logarithmic law while providing  
 284 numerical stability for FVM scheme. For instance, in evaluating the production term  $P_k|_c$  in  
 285 (2.11), the friction velocity to the power three is often split into two contributions: turbulence  
 286 and the mean flow shears.



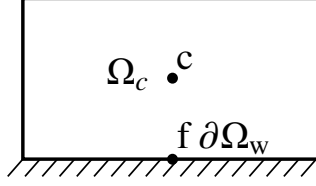


Figure 1: First grid cell close to the wall.

287

## 2.3. A continuous adjoint RANS model

288

The optimisation problem (2.1) can be solved by augmenting the cost function with the constraint, *i.e.* the RANS model. This is done through Lagrange multipliers also called adjoint variables. The resulting unconstrained optimisation problem can be written in a compact form as

292

$$\mathcal{L}(\mathbf{X}, \mathbf{X}^*, \alpha) = \mathcal{J}(P, \alpha) + \langle \mathbf{X}^*, \mathbf{M}(\mathbf{X}, \alpha) \rangle_{\Omega}, \quad (2.15)$$

293

where  $\langle \cdot, \cdot \rangle_{\Omega}$  stands for the spatial  $L^2$  inner-product in the flow domain  $\Omega$ . The mean flow state  $\mathbf{X}$  is defined by the set  $(\mathbf{U}, P, k, \epsilon, \mu_t)$ . As for the adjoint state  $\mathbf{X}^*$ , we define it as  $(\mathbf{U}^*, P^*, k^*, \epsilon^*, \mu_t^*)$ . The term  $\mathbf{U}^*$  stands for the adjoint velocity,  $P^*$  is the adjoint pressure field,  $k^*$  is the adjoint turbulent kinetic energy,  $\epsilon^*$  the adjoint kinetic dissipation rate and  $\mu_t^*$  the adjoint eddy-viscosity.

298

Solving the optimisation problem implies to find the set of parameters, the state vector and the adjoint state such that the derivatives of  $\mathcal{L}$  with respect to all variables vanish. To this end, based on the application of the Green-Gauss theorem and the use of integrations by parts – see the Appendix and the work of (Othmer 2008)– the adjoint system reads as follows:

303

$$-\rho \frac{\partial U_j U_i^*}{\partial x_j} - \rho U_j \frac{\partial U_j^*}{\partial x_i} - \frac{\partial}{\partial x_j} \left[ \mu_{eff} \left( \frac{\partial U_i^*}{\partial x_j} + \frac{\partial U_j^*}{\partial x_i} \right) \right] + \frac{\partial P^*}{\partial x_i} = D_{U^*,i} \quad (2.16)$$

304

$$\frac{\partial U_j^*}{\partial x_j} = 0 \quad (2.17)$$

305

$$-\frac{\partial \rho U_j k^*}{\partial x_j} - \frac{\partial}{\partial x_i} \left[ \left( \mu + \frac{\mu_t}{\sigma_k} \right) \frac{\partial k^*}{\partial x_j} \right] - \rho \frac{2}{3} \frac{\partial U_i}{\partial x_i} k^* = D_{k^*} \quad (2.18)$$

306

$$-\frac{\partial \rho U_j \epsilon^*}{\partial x_j} - \frac{\partial}{\partial x_i} \left[ \left( \mu + \frac{\mu_t}{\sigma_{\epsilon}} \right) \frac{\partial \epsilon^*}{\partial x_j} \right] - \rho \frac{\partial P_{\epsilon}}{\partial \epsilon} \epsilon^* + \rho \frac{\partial s_{\epsilon}}{\partial \epsilon} \epsilon^* = D_{\epsilon^*} \quad (2.19)$$

307

308

$$\frac{\partial P_k}{\partial \mu_t} k^* - \left( \frac{\partial U_i}{\partial x_j} + \frac{\partial U_j}{\partial x_i} \right) \frac{\partial U_j^*}{\partial x_i} - \frac{1}{\sigma_k} \frac{\partial k}{\partial x_i} \frac{\partial k^*}{\partial x_i} - \frac{1}{\sigma_{\epsilon}} \frac{\partial \epsilon}{\partial x_i} \frac{\partial \epsilon^*}{\partial x_i} = \mu_t^*. \quad (2.20)$$

The right-hand sides are expressed as

$$D_{U^*,i} = k \frac{\partial k^*}{\partial x_i} + \epsilon \frac{\partial \epsilon^*}{\partial x_i} + \frac{2}{3} \frac{\partial k k^*}{\partial x_i} - \frac{\partial P_{\epsilon}}{\partial U_i} \epsilon^* - \frac{\partial P_k}{\partial U_i} k^* - \frac{\partial}{\partial x_i} \left( \frac{\partial \mu_t}{\partial U_i} \mu_t^* \right)$$

$$D_{k^*} = \rho \frac{\partial P_{\epsilon}}{\partial k} \epsilon^* - \rho \frac{\partial s_{\epsilon}}{\partial k} \epsilon^* - \frac{\partial \mu_t}{\partial k} \mu_t^*$$

$$D_{\epsilon^*} = -\frac{\partial \mu_t}{\partial \epsilon} \mu_t^*,$$

309

where  $P_k$  and  $P_{\epsilon}$  stand for the production terms of turbulent energy (second term in the

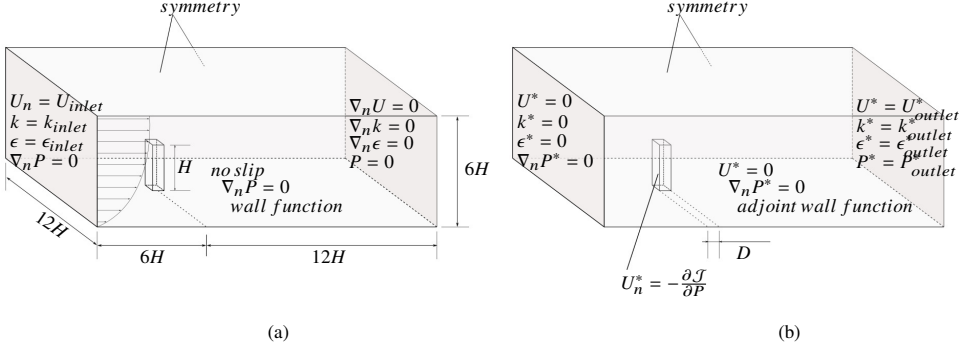


Figure 2: Settings and boundary conditions of flow solution (a) and adjoint solution (b).

310 RHS of (2.7)) and for the turbulence dissipation rate (second term in the RHS of (2.8)),  
 311 respectively. As for  $s_\epsilon$ , it denotes the modeled sink of turbulence dissipation rate (third term  
 312 in the RHS of (2.8)). To solve this adjoint system, adjoint boundary conditions have to be  
 313 derived consistently with the boundary conditions of the direct problem. The next section is  
 314 dedicated to this crucial point.

#### 315 2.4. Adjoint boundary conditions

316 The treatment of the adjoint boundary conditions is a central piece in adjoint methods in order  
 317 to obtain consistency in the gradient computation. In our case with the transport equations  
 318 of turbulent quantities, some treatments are not standard, particularly at the adjoint wall  
 319 law. Moreover, some specific treatments are performed at the discrete level of the finite  
 320 volume formulation. In this section, we propose to recall the general procedure to obtain  
 321 adjoint boundary conditions, and then to detail the conditions to enforce at each boundary.  
 322 Boundary conditions for the flow and adjoint fields are summarised in figure 2.

323 Derivation of (2.15) leads, in addition to system (2.16)-(2.19), to a system of boundary  
 324 terms. Directional derivative with respect to  $P$ , leads to

$$325 \quad [U_i^* n_i \delta P]_{\delta\Omega} = -\frac{\partial J}{\partial P} \delta P, \quad (2.21)$$

326 where the boundary integral is defined as  $[\cdot]_{\delta\Omega} = \int_{\partial\Omega} (\cdot) d\delta\Omega$ . By deriving with respect to  
 327  $U_i$ , we obtain

$$329 \quad \begin{aligned} & [P^* \delta U_i n_i]_{\delta\Omega} - \left[ \rho \left( (U_i^* n_i) (U_i n_i) + U_j U_j^* n_i \right) \delta U_i n_i \right]_{\delta\Omega} - \left[ \mu_{eff} (U_i^* n_i + U_j^* n_j) \frac{\partial \delta U_i}{\partial x_j} \right]_{\delta\Omega} \\ & - \left[ \delta U_i \mu_{eff} \left( \frac{\partial U_i^* n_i}{\partial x_j} n_i + \frac{\partial U_j^* n_j}{\partial x_i} n_i \right) \right]_{\delta\Omega} \\ & - \left[ \delta U_i \left( \frac{5}{3} \rho k k^* n_i + \left( \frac{\partial P_k}{\partial U_j} n_i \right) k^* + \rho \epsilon \epsilon^* n_i + \left( \frac{\partial P_\epsilon}{\partial U_j} n_i \right) \epsilon^* + \left( \frac{\partial \mu_t}{\partial U_j} n_i \right) \mu_t^* \right) \right]_{\delta\Omega}. \end{aligned} \quad (2.22)$$

330 Derivative with respect to  $k$ , leads to

$$\left[ -\frac{2}{3}\rho U_i^* n_i \delta k \right]_{\delta\Omega} + [\rho U_i n_i k^* \delta k]_{\delta\Omega} - \left[ \left( \mu + \frac{\mu_t}{\sigma_k} \right) k^* \frac{\partial \delta k}{\partial x_j} n_j \right]_{\delta\Omega} + \left[ \frac{\partial \left( \mu + \frac{\mu_t}{\sigma_k} \right) k^*}{\partial x_j} n_j \delta k \right]_{\delta\Omega}, \quad (2.23)$$

331  
332 and with respect to  $\epsilon$  to

$$[\rho U_i n_i \epsilon^* \delta \epsilon]_{\delta\Omega} - \left[ \left( \mu + \frac{\mu_t}{\sigma_k} \right) \epsilon^* \frac{\partial \delta \epsilon}{\partial x_j} n_j \right]_{\delta\Omega} + \left[ \frac{\partial \left( \mu + \frac{\mu_t}{\sigma_k} \right) \epsilon^*}{\partial x_j} n_j \delta \epsilon \right]_{\delta\Omega}. \quad (2.24)$$

334 Finally by deriving with respect to  $\mu_t$ , we obtain

$$\left[ \delta \mu_t \left( \mu_t^* - \left( \frac{\partial U_j}{\partial x_i} n_j + \frac{\partial U_i}{\partial x_j} n_j \right) U_i^* - \frac{\rho}{\sigma_k} k^* \frac{\partial k}{\partial x_j} n_j - \frac{\rho}{\sigma_\epsilon} \epsilon^* \frac{\partial \epsilon}{\partial x_j} n_j \right) \right]_{\delta\Omega}. \quad (2.25)$$

336 Then at each boarder, variations of the direct boundary conditions are injected in the  
337 system (2.21)–(2.25), to obtain the corresponding adjoint boundary conditions.

338 At the inlet, the direct boundary conditions lead to

$$339 \quad \delta U_i t_i = 0 \quad ; \quad \delta U_i n_i = 0 \quad ; \quad \delta k = 0 \quad ; \quad \delta \epsilon = 0. \quad (2.26)$$

340 Substituting this in (2.21)–(2.24), the system reduces to

$$341 \quad U_i^* t_i = 0 \quad ; \quad U_i^* n_i = 0 \quad ; \quad k^* = 0 \quad ; \quad \epsilon^* = 0. \quad (2.27)$$

342 This quite standard result at the continuous level is not straightforward to implement in the  
343 finite volume formulation. No condition is imposed on  $P^*$  and the inlet boundary condition  
344 for the adjoint pressure is left arbitrary. But, in accordance with (Zymaris *et al.* 2010;  
345 Othmer 2008) and identically as the numerical treatment of the direct inlet pressure  $P$ , zero  
346 Neumann condition on  $P^*$  is imposed to ensure numerical stability. To obtain the other  
347 boundary conditions, the same approach is employed.

348 At the outlet, the pressure value is prescribed while the other flow variables have their  
349 normal gradient imposed, leading to

$$P^* n_i = (U_i^* n_i)(U_i n_i) + (U_j^* U_j) n_i + 2 * \mu_{eff} \frac{\partial (U_j^* n_j)}{\partial x_i} n_i + \frac{5}{3} \rho k k^* n_i + \rho \epsilon \epsilon^* n_i + \left( \frac{\partial \mu_t}{\partial U_j} n_j \right) n_i \mu_t^*. \quad (2.28)$$

350  
351 This provides a constraint on the boundary condition to determine the adjoint pressure at the  
352 outlet. In equation (2.28), the adjoint pressure at the next iteration is determined explicitly  
353 by evaluating  $U^*$  at the previous iteration. Projecting then the fluxes on the outlet tangent  
354 plane, we obtain:

$$355 \quad \mu_{eff} \frac{\partial (U_j^* t_j)}{\partial x_i} n_i + (U_i^* t_i)(U_i n_i) = - \left( \frac{\partial \mu_t}{\partial U_i} n_i \right) t_i \mu_t^* - \left( \frac{\partial P_k}{\partial U_j} n_j \right) t_i k^* - \left( \frac{\partial P_\epsilon}{\partial U_j} n_j \right) t_i \epsilon^*. \quad (2.29)$$

356 This equation provides a boundary condition for the tangential component of the adjoint  
357 velocity.

358 It is worth noting that, instead, an alternative choice could be made by imposing  $P^* = 0$   
359 and determining the adjoint velocity by solving equations (2.28) and (2.29). Previous works,  
360 for a different turbulence model (Zymaris *et al.* 2010) or for frozen turbulence assumption  
361 (Othmer 2008), showed that both implementations yields to identical sensitivities.

362 Derivation w.r.t.  $k$ ,  $\epsilon$  and  $\mu_t$  leads, respectively, to

$$363 \quad \rho k^* U_i n_i + \rho D_k \frac{\partial k^*}{\partial x_i} n_i = \frac{\partial \mu_t}{\partial k} \mu_t^*, \quad (2.30)$$

$$364 \quad \rho \epsilon^* U_i n_i + \rho D_\epsilon \frac{\partial \epsilon^*}{\partial x_i} n_i = \frac{\partial \mu_t}{\partial \epsilon} \mu_t^*, \quad (2.31)$$

$$365 \quad \left( \frac{\partial U_j}{\partial x_i} n_j + \frac{\partial U_i}{\partial x_j} n_j \right) U_i^* = \mu_t^*. \quad (2.32)$$

366

367 Therefore, for known outlet direct and adjoint velocities, the adjoint eddy viscosity is updated  
368 through equation (2.32). Then, conditions (2.30) and (2.31) can be imposed to solve  $k^*$  and  
369  $\epsilon^*$  respectively.

370 As for the side and top free-stream boundaries under symmetry condition, we assume a  
371 zero flux of all flow variables,

$$372 \quad \frac{\partial P}{\partial x_i} n_i = \frac{\partial (U_j t_j)}{\partial x_i} n_i = \frac{\partial k}{\partial x_i} n_i = \frac{\partial \epsilon}{\partial x_i} n_i = 0, \quad (2.33)$$

373 and zero normal velocity,

$$374 \quad U_i n_i = 0. \quad (2.34)$$

375 We thus obtain the following boundary conditions for the adjoint variables:

$$376 \quad U_i^* n_i = 0, \quad \frac{\partial (U_i^* t_i)}{\partial x_j} n_j = 0, \quad \frac{\partial k^*}{\partial x_i} n_i = 0, \quad \frac{\partial \epsilon^*}{\partial x_i} n_i = 0, \quad \mu_t^* = 0. \quad (2.35)$$

377 This shows that symmetric boundary conditions are conserved with the adjoint model.

378 The wall boundaries are split into two parts, namely  $\partial\Omega_{\text{tower}}$  for the part where data are  
379 provided, *i.e.* the tower, and  $\partial\Omega_{\text{gr}}$  for the walls at the ground modelling the surrounding  
380 environment, for which there is no data. Based on equation (2.21) we have

$$381 \quad U_i^* n_i = \frac{\partial \mathcal{J}}{\partial P} \quad \text{at} \quad \partial\Omega_{\text{tower}}, \quad (2.36)$$

$$382 \quad U_i^* n_i = 0 \quad \text{at} \quad \partial\Omega_{\text{gr}}, \quad (2.37)$$

$$383 \quad U_i^* t_i = 0 \quad \text{at} \quad \partial\Omega_{\text{tower}} \cup \partial\Omega_{\text{gr}}. \quad (2.38)$$

385 Therefore exactly in the same way as for the inlet, the no-slip condition on the velocity,  
386 associated with a zero Neumann condition on the mean pressure, implies a homogeneous  
387 Dirichlet boundary condition for the adjoint velocity and a zero Neumann condition for  
388 the adjoint pressure at the ground walls  $\partial\Omega_{\text{gr}}$ . Let us note that due to the wall-pressure  
389 measurements, the Dirichlet condition on the adjoint variable  $U^*$  is inhomogeneous on the  
390 normal component along  $\partial\Omega_{\text{tower}}$  at the sensor positions.

391 Considering the adjoint turbulence variables ( $k^*$ ,  $\epsilon^*$ ,  $\mu_t^*$ ), it is important to consider the  
392 expression of the wall-law in order to derive their boundary conditions. From the equality  
393 (2.13), the log law is imposed by re-evaluating the wall viscous fluxes through a prescribed  
394 value of the eddy-viscosity. From the relations

$$395 \quad U^+ = \frac{1}{\kappa} \ln(E y^+) \quad \text{at} \quad \partial\Omega_{\text{tower}},$$

396 and

$$397 \quad U^+ = \frac{1}{\kappa} \ln\left(\frac{y + z_0}{z_0}\right) \quad \text{at} \quad \partial\Omega_{\text{gr}},$$

398 the eddy viscosity is then defined such that

$$399 \quad \mu_t = \mu \left( \frac{y^+ \kappa}{\ln(E y^+)} - 1 \right) \quad \text{at} \quad \partial\Omega_{\text{tower}}, \quad (2.39)$$

$$400 \quad \mu_t = \mu \left( \frac{y^+ \kappa}{\ln\left(\frac{y^+ z_0}{z_0}\right)} - 1 \right) \quad \text{at} \quad \partial\Omega_{\text{gr}}, \quad (2.40)$$

402 where  $E = 9.8$  is the roughness parameter for smooth walls (Versteeg & Malalasekera 2007)  
 403 and  $z_0 = 0.02$  m is the roughness length which is relevant for an ABL flow scale. Recalling  
 404 from figure 1 that  $|_c$  and  $|_f$  denote respectively the first cell centre and the boundary face  
 405 values, on both walls  $\mu_t|_f$  is seen to be dependent on  $k|_c$  solely. Furthermore, by imposing the  
 406 inertial balance (2.11) we observe that  $\epsilon|_c$  is an explicit function of  $k|_c$ . As a consequence,  
 407 we conclude that the logarithmic wall-closure can actually be defined uniquely through the  
 408 knowledge of the turbulent kinetic energy value at the first cell-center only. We propose thus  
 409 to reconsider the derivation of these terms inside the domain included in the cells adjacent to  
 410 the wall. Replacing  $\epsilon|_c$  by its function of  $k|_c$  (equation (2.11)), we are led to consider a zero  
 411 Neumann boundary condition, which is fully consistent with the homogeneity assumption  
 412 near the wall. This yields to the following modification to the sources terms at the wall  
 413 adjacent cell

$$414 \quad D_{k^*} = \rho \frac{\partial P_\epsilon}{\partial k} \epsilon^* - \rho \frac{\partial s_\epsilon}{\partial k} \epsilon^* + \rho \left( \frac{\partial P_k}{\partial k} |_c - \frac{\partial \epsilon}{\partial k} |_c \right) k^* |_c \quad \text{and} \quad D_{\epsilon^*} = 0 \quad \text{in} \quad \Omega_c, \quad (2.41)$$

415 with  $P_\epsilon$  and  $s_\epsilon$ , the dissipation production and sink terms, being modified accordingly. At  
 416 the continuous level, the third term in the RHS vanishes assuming turbulence homogeneity.  
 417 However, at the discrete level, as discussed in section 2.2, it is kept for numerical consistency.

418 Furthermore, as we impose a homogeneous Neumann boundary condition for  $k$  in equation  
 419 (2.10), it can be observed that this leads to the same set of conditions as in the outlet (equations  
 420 (2.30), (2.31) and (2.32)). Moreover, with the no slip condition and the set of conditions for  
 421 the adjoint velocity ((2.36), (2.37), (2.38)), the wall boundary conditions for the adjoint  
 422 dissipation rate and eddy viscosity reads as

$$423 \quad \frac{\partial \epsilon^*}{\partial x_i} n_i = 0 \quad \text{at} \quad \partial\Omega_{\text{tower}} \cup \partial\Omega_{\text{gr}}, \quad (2.42)$$

$$424 \quad \mu_t^* = 2 \left( \frac{\partial(U_i n_i)}{\partial x_j} n_j \right) U_i^* n_i \quad \text{at} \quad \partial\Omega_{\text{tower}}, \quad (2.43)$$

$$425 \quad \mu_t^* = 0 \quad \text{at} \quad \partial\Omega_{\text{gr}}. \quad (2.44)$$

427 Concerning the boundary condition on  $k^*$ , we propose to consider (2.30) at  $|_c$  while we  
 428 impose zero Neumann condition at  $|_f$ . This leads to the following boundary condition for  $k^*$ :

$$429 \quad \frac{\partial k^*}{\partial x_j} n_j |_f = 0 \quad \text{at} \quad \partial\Omega_w \quad (2.45)$$

430 and

$$431 \quad k^* |_c = \frac{\partial \mu_t}{\partial k} |_f \frac{\mu_t^* |_f}{\rho U_i n_i} \quad \text{in} \quad \Omega_c. \quad (2.46)$$

432 Some numerical tests have shown that this alternative solution led to identical results on  
 433 the initial sensitivity field than the non-homogeneous Neumann boundary condition. Hence,  
 434 with this treatment, wall conditions for the adjoint system are now fully consistent with the  
 435 initial RANS model and leads us thus to a consistent minimisation procedure.

436 Now that we have at our disposal a dual description of the dynamics composed of a  
 437 RANS direct model and the adjoint of its tangent linear representation, we explore three  
 438 methodological settings for an in-depth diagnosis of the turbulence closure. The first tool at  
 439 hand consists simply to inspect the adjoint state maps. The second one consists in optimising  
 440 global constants parameters of the turbulence model for reducing the observation error; and  
 441 to relax/enforce constraints on these parameters to test physical hypotheses. The last one,  
 442 goes one step further and considers the adjunction of distributed unknowns which enables to  
 443 identify a missing term in the equation where the turbulence closure is performed, here, in the  
 444 transport equation for the energy dissipation rate. In order to conduct an efficient structural  
 445 inspection, distributed parameter is sought in the Sobolev space and further estimated through  
 446 a data-assimilation procedure. These three settings are described in section 3 and applied  
 447 then to a high-rise building case study described section 4. The numerical results on this  
 448 case study for the three different sensitivity analyses are presented in section 5.

### 449 3. Adjoint-based diagnostic tool for turbulence models

450 In the previous section we detailed the construction of a continuous adjoint model (together  
 451 with its consistent boundary conditions) of the tangent linear operator of a RANS model for  
 452 very high Reynolds flow, associated with large integral/body length scales. In the current  
 453 section, we present methodological tools derived from this adjoint operator. Beyond providing  
 454 a data-driven flow reconstruction, it enables us an in-depth analysis of the turbulence closure.

#### 455 3.1. Adjoint state as a basis for sensitivity analysis

While in general, adjoint variables are usually considered as a purely mathematical object,  
 they do have physical meaning which have been explored in several works (Hall & Cacuci  
 1983; Giles & Pierce 2000; Gunzburger 2003). Although we know that RANS models (at  
 least with Boussinesq eddy viscosity hypothesis for its closure) does not allow an accurate  
 representation of complex flows, they nevertheless provide some usefull global insights on the  
 flow. With this in mind, the reconstructed adjoint state enables to highlight a misrepresentation  
 of the turbulent flow by the RANS model, hence, pointing where it is possible to optimise  
 the RANS model parameters to optimally reduce the difference between the CFD state and a  
 given experimental dataset. Moreover, from an optimisation perspective, one may interpret  
 them as a steepest descent direction of an objective cost function, for a particular control  
 parameter. For instance, the adjoint velocity can be seen as the influence of an arbitrary  
 forcing  $\mathbf{f}_u$  acting on the mean momentum equation. This can be shown when deriving an  
 optimality condition by a perturbation of this force,

$$\begin{aligned} \mathbf{M}_u(\mathbf{X}, \alpha) = \mathbf{f}_u & \quad \rightarrow \quad \frac{\partial \mathcal{J}}{\partial \mathbf{f}_u} = \mathbf{U}^*. \\ \text{Momentum equation} & \quad \rightarrow \quad \text{Optimality condition.} \end{aligned}$$

456 Then, as we perform a first update of this forcing by a gradient-descent minimisation  
 457 algorithm, one obtain

$$458 \quad \mathbf{f}_u^{it_1} = (\mathbf{f}_u^{it_0} = 0) - \lambda \mathbf{U}^*,$$

while  $\lambda$  is a positive non-dimensional marching step factor. Through dimensional analysis,  
 one may scale  $\mathbf{U}^*$ , which has the dimension of an acceleration, as  $U^* \sim \frac{U_{\text{ref}}^2}{H_{\text{ref}}}$ . The adjoint  
 velocity features are thus immediately representing a missing term, that can be interpreted  
 as a correction of the Reynolds stress. Examining the adjoint turbulence variables of a  $k - \epsilon$   
 model, namely  $k^*$ ,  $\epsilon^*$  and  $\mu_t^*$ , similar interpretations can be drawn as we consider arbitrary

forcing such as

$$\begin{aligned}
 M_k(\mathbf{X}, \alpha) = f_k &\quad \rightarrow \quad \frac{\partial \mathcal{J}}{\partial f_k} = k^*, \\
 M_\epsilon(\mathbf{X}, \alpha) = f_\epsilon &\quad \rightarrow \quad \frac{\partial \mathcal{J}}{\partial f_\epsilon} = \epsilon^*, \\
 M_{\mu_t}(\mathbf{X}, \alpha) = f_{\mu_t} &\quad \rightarrow \quad \frac{\partial \mathcal{J}}{\partial f_{\mu_t}} = \mu_t^*.
 \end{aligned}$$

459 The adjoint variables shed some light on the flow regions that are sensitive to an eventual  
 460 correction of the turbulence model. As this will be shown in the case study of section 5,  
 461 this interpretation is very helpful to analyze the incorporation of additional variables to  
 462 define efficient data-driven turbulence closure. These forcings can indeed be associated to  
 463 any of modeled terms meant to address a particular turbulence modelling error (e.g. energy  
 464 production, backscattering, redistribution or dissipation). The sensitivity of the associated  
 465 parametric shapes and hyper-parameter can be efficiently obtained and inspected through the  
 466 adjoint operator.

### 467 3.2. Adjoint diagnosis on global closure coefficients

468 Given the adjoint dynamics, the sensitivity of any parameter can be obtained from the  
 469 optimality condition (6.3). Free constants of the RANS model can be finely tuned knowing  
 470 their sensitivities. As we will show for a particular turbulence model (realizable  $k - \epsilon$ ), the  
 471 quality of the associated numerical reconstructions appears to be quite restricted, for a range  
 472 of physically acceptable values of these parameters. The reason of the inefficiency of the  
 473 calibration procedure is interpreted below in terms of a too strong model “rigidity”. This  
 474 hindering facts will be later illustrated when we will perform the sensitivity analysis and data  
 475 assimilation on the high-rise building case.

#### 476 3.2.1. A sensitivity field

477 Considering the vector  $\alpha = (A_0, C_2, \sigma_k, \sigma_\epsilon)$  of closure parameters, the optimality con-  
 478 dition (6.3) is obtained by differentiating the Lagrangian (2.15) in the directions  $\delta\alpha =$   
 479  $(\delta A_0, \delta C_2, \delta\sigma_k, \delta\sigma_\epsilon)$ :

$$\begin{aligned}
 \frac{\partial \mathcal{L}}{\partial A_0} \delta A_0 &= \left\langle \frac{\partial M_{\mu_t}}{\partial A_0} \delta A_0, \mu_t^* \right\rangle_\Omega = \langle -\mu_t C_\mu \delta A_0, \mu_t^* \rangle_\Omega = \langle -\mu_t C_\mu, \mu_t^* \rangle_\Omega \delta A_0 \\
 \frac{\partial \mathcal{L}}{\partial C_2} \delta C_2 &= \left\langle \frac{\epsilon^2}{k + \sqrt{\mu \epsilon}}, \epsilon^* \right\rangle_\Omega \delta C_2 \\
 \frac{\partial \mathcal{L}}{\partial \sigma_k} \delta \sigma_k &= \left\langle -\frac{\partial}{\partial x_j} \left[ \frac{\mu_t}{\sigma_k^2} \frac{\partial k}{\partial x_i} \right], k^* \right\rangle_\Omega \delta \sigma_k \\
 \frac{\partial \mathcal{L}}{\partial \sigma_\epsilon} \delta \sigma_\epsilon &= \left\langle -\frac{\partial}{\partial x_j} \left[ \frac{\mu_t}{\sigma_\epsilon^2} \frac{\partial \epsilon}{\partial x_i} \right], \epsilon^* \right\rangle_\Omega \delta \sigma_\epsilon.
 \end{aligned} \tag{3.1}$$

481 So far, this does not include any explicit dependency of the cost on the set of parameters, such  
 482 as a penalisation term. It can be observed that the optimality conditions reduce drastically  
 483 the high dimensional dependency of the model to the lower dimensional parameter space.  
 484 This reduction, performed via the inner product  $\langle \cdot, \cdot \rangle_\Omega$ , does reflect the global compromising  
 485 character of the closure coefficients. This results in a rather rigid situation when seeking data-  
 486 model fitting. However, this rigidity can be understood as a strong confidence in the model

487 structure. This strongly constrains the solutions but enables, on the other hand, to assimilate  
 488 very sparse measurements. The examination of the spatially varying adjoint variables to  
 489 diagnose the parameter sensitivity provides useful piece of information even though we deal  
 490 with a rigid parametric model for the reconstruction. This type of analysis will be exploited  
 491 in our case study.

### 492 3.2.2. Penalty range

493 To ensure realistic numerical solutions, relevant physical range for each of the closure  
 494 coefficients is defined. These constraints are introduced via penalty terms on the control  
 495 parameters through an error covariance matrix, in cost function (2.2). Values of the parameters  
 496 outside of a range defined by the standard deviation are hence strongly penalised. These  
 497 standard deviations are in practice fixed from experiments on prototypical configurations  
 498 of boundary layer or decaying turbulence. This may become questionable in regions where  
 499 the fluid and building interact and near flow separations associated with strong shears. As  
 500 a matter of fact, the assumptions underlying the concept of eddy viscosity starts to be  
 501 less reasonable in these regions (Pope 2001). Thus, as a compromise, the range limits are  
 502 fixed from experiments as intervals  $\Delta\alpha_i$  centered around the background a priori value. The  
 503 covariance matrix is finally expressed as follows

$$504 \quad B_{ii}^{-1} = \zeta_i \left( \frac{|\frac{\partial \mathcal{J}_0}{\partial \alpha}|}{\Delta\alpha_i} \right).$$

505 As mentioned earlier, this covariance has two roles: first, to impose the trusted (or recom-  
 506 mended) ranges  $\Delta\alpha_i$  and secondly, to ensure a dimensional homogeneity of the cost function  
 507 through the norm of the sensitivity derivative given at the first minimisation iteration  $|\frac{\partial \mathcal{J}_0}{\partial \alpha}|$ .  
 508 The importance of control variables with high values of sensitivity derivatives is strengthen  
 509 in the objective function in comparison to less sensitive parameters. The parameters  $\zeta_i$  are  
 510 dimensionless free parameters allowing to give more or less global *a priori* confidence on  
 511 each parameter. In practice these parameters can be fixed from a priori considerations.

### 512 3.3. Adjoint diagnosis on spatially distributed closure: correction in the dissipation 513 transport equation

514 In contrast to the previous section, we consider now the adjoint system as a basis for  
 515 the inspection of the model misrepresentations through a distributed parameter. Instead of  
 516 correcting coefficients of the model, we consider here the adjunction of a force to one of  
 517 the model equations. We consider a corrective forcing term at the level of the dissipation  
 518 transport equation, where the closure take place. Then, with the aim to further investigate  
 519 such a closure through a data-assimilation procedure, a specific optimisation in the  $H^1(\Omega)$   
 520 Sobolev space is proposed in order to provide a regularisation procedure that guaranties an  
 521 efficient descent direction as well as an implicit spatial smoothing of the forcing. With this  
 522 regularisation, a significant improvement of the results will be shown in our study case.

#### 523 3.3.1. A corrective model

524 As it was noted in the previous section, due to the model rigidity arising from the drastically  
 525 small parameter space, the flow is not free to visit a sufficiently large domain of the state  
 526 space that is too far from the basic RANS model. To overcome such restrictions, one  
 527 may straightforwardly consider a set of closure parameters with a higher dimension. Still  
 528 maintaining the validity of the Boussinesq approximation, a strategy consists in enriching  
 529 the turbulence model structure. We choose to add a forcing term in the transport equation  
 530 of  $\epsilon$  (equation (2.8)) in order to correct what we may call structural errors, *i.e.* error arising



531 from the choice of the turbulence model equation. We could have considered as well a  
 532 control parameter defined directly as the forcing of equation (2.8), however, we preferred to  
 533 introduce some dependency of this forcing to the state variable. We choose a forcing term  
 534 of the form  $-f_\epsilon \epsilon$ , where  $f_\epsilon$  is the control parameter. The sign convention is chosen so as the  
 535 added forcing corresponds to a sink of dissipation. The objective of the pre-multiplication  
 536 by  $\epsilon$  is to prevent unphysical dissipation corrections at locations where there is no turbulence  
 537 and to focus specifically on relevant regions such as the shear layers and the wake. Numerical  
 538 tests presented in section 5.3.1, demonstrate that this term behaves indeed much better than a  
 539 direct forcing term. With this additional forcing, the dissipation transport equation becomes

$$540 \quad \frac{\partial \rho U_j \epsilon}{\partial x_j} - \frac{\partial}{\partial x_j} \left[ \left( \mu + \frac{\mu_t}{\sigma_\epsilon} \right) \frac{\partial \epsilon}{\partial x_i} \right] - C_1(S, k, \epsilon) S \epsilon + C_2 \frac{\epsilon^2}{k + \sqrt{\mu \epsilon}} = -f_\epsilon \epsilon. \quad (3.2)$$

541 This model remains close to the RANS structure as to avoid overfitting effects in the context  
 542 of severe differences between the state space and measurements.

### 543 3.3.2. Sensitivity field

544 The fact that the added distributed parameter depends on the state variable  $\epsilon$ , requires some  
 545 modifications of the adjoint equations. In compact form, the adjoint equation on  $\epsilon^*$  reads  
 546 now as

$$547 \quad M_{\epsilon^*} = -f_\epsilon \epsilon^*, \quad (3.3)$$

where  $M_{\epsilon^*}$  contains all the adjoint terms derived from equation (2.19). Regarding the adjoint  
 boundary conditions, since no face flux are involved through the additive term, no changes  
 have to be made. The optimality condition associated with the control parameter  $f_\epsilon$  is obtained  
 by considering the directional derivative

$$\left\langle \frac{\partial \mathcal{L}}{\partial f_\epsilon}, \delta f_\epsilon \right\rangle_\Omega = \langle \epsilon \delta f_\epsilon, \epsilon^* \rangle_\Omega,$$

548 leading straightforwardly to express the Lagrangian sensitivity to  $f_\epsilon$  as

$$549 \quad \frac{\partial \mathcal{L}}{\partial f_\epsilon} = \epsilon \epsilon^*. \quad (3.4)$$

550

### 551 3.3.3. Descent direction

With very sparse partial observations and the consideration of spatially distributed control  
 parameters, the risks of obtaining local minima or unphysical flow reconstructions is much  
 stronger. The control parameter can be any function of  $L^2(\Omega)$ , which allows highly irregular  
 functions. Regularisation is a classical way to reduce the number of local minima eventually  
 associated to unphysical solutions. To that purpose, penalty of the spatial gradients of  
 the control parameter is often considered (Franceschini *et al.* 2020). Such regularisations  
 introduces a smoothing penalty parameter on which the solution strongly depends and whose  
 value is in general non-trivial to choose. In the following, we consider as an alternative a  
 Sobolev gradient regularisation (Protas *et al.* 2004; Tissot *et al.* 2020). It consists to define  
 the control parameter in the Sobolev space  $H^1(\Omega)$  which is more regular than  $L^2(\Omega)$ . With  
 this approach the functional is still defined in its basic form as

$$\mathcal{J}(P) = \frac{1}{2} \|\rho U_{\text{ref}}^2 \Delta C_p\|_{R^{-1}}^2.$$

552 Provided the optimality condition (3.4) and for an arbitrary functions  $\psi$  and  $\phi$  in  $H^1(\Omega)$ , the  
 553 Sobolev gradient is defined such that

$$554 \quad \left\langle \frac{\partial \mathcal{L}}{\partial f_\epsilon}, \psi \right\rangle = \left\langle \frac{\partial \mathcal{L}^{H^1}}{\partial f_\epsilon}, \psi \right\rangle_{H^1}, \quad (3.5)$$

555 with the inner product definition

$$\langle \phi, \psi \rangle_{H^1} = \int_{\Omega} \phi \psi + l_{sob}^2 (\nabla \phi \cdot \nabla \psi) d\Omega,$$

556 in which  $l_{sob}^2$  is a free parameter. Through integration by part of the second term of the inner  
 557 product (involving the function at gradients), the equality (3.5) leads to the new optimality  
 558 condition

$$559 \quad \frac{\partial \mathcal{L}^{H^1}}{\partial f_\epsilon} = \left( \frac{1}{1 + l_{sob}^2} (\mathbb{I} - l_{sob}^2 \nabla^2) \right)^{-1} \frac{\partial \mathcal{L}}{\partial f_\epsilon}, \quad (3.6)$$

561 in which  $\nabla^2$  stands for the Laplacian operator. Equation (3.6) is a projection of the sensitivity  
 562 in  $L^2(\Omega)$  onto the Sobolev space. With this approach, the sensitivity field is consequently  
 563 regularised through the solution of an Helmholtz equation. Since Matrix inversion is not an  
 564 option in such large system, the Poisson equation (3.6) is here solved through an iterative  
 565 technique expressed within the same finite volume scheme as for the direct RANS equations.  
 566 It is worth to mention that this type of formulation offers two main advantages compared to  
 567 classical regularisation terms. In the one hand, as opposed to the global penalty coefficient  
 568 introduced in those latter, the free parameter involved in the projection approach is indeed  
 569 a physical quantity. As a matter of fact, it is easy to see through dimensional analysis of  
 570 (3.6) that  $l_{sob}$  has the dimensions of a length. More precisely this parameter can be seen as  
 571 a filtering length scale below which the sensitivity field is smoothed. It provides us a way  
 572 to introduce a characteristic length scale relevant with the flow (*e.g.*, the building width for  
 573 instance). In the other hand, the Sobolev gradient does ensure a descent direction. Indeed,  
 574 applying a Taylor expansion of the cost function around an initial guess  $f_\epsilon$  in the direction  
 575  $\delta f_{eps} = -\frac{\partial \mathcal{L}^{H^1}}{\partial f_\epsilon}$  can be expressed as follows

$$576 \quad \mathcal{J}(f_\epsilon + h\delta f_\epsilon) = \mathcal{J}(f_\epsilon) + h \left\langle \frac{\partial \mathcal{L}}{\partial f_\epsilon}, \delta f_\epsilon \right\rangle + \mathcal{O}(h^2).$$

577 Substituting the second term in the RHS by using the equality (3.5) yields to

$$578 \quad \mathcal{J}(f_\epsilon + h\delta f_\epsilon) = \mathcal{J}(f_\epsilon) - h \left\| \frac{\partial \mathcal{L}^{H^1}}{\partial f_\epsilon} \right\|_{H^1}^2 + \mathcal{O}(h^2),$$

579 in which we define the norm  $\|a\|_{H^1}^2 = \langle a, a \rangle_{H^1}$ . Thus, for a small enough perturbation  $h\delta f_\epsilon$ ,  
 580 we have  $\mathcal{J}(f_\epsilon + h\delta f_\epsilon) < \mathcal{J}(f_\epsilon)$ . Now, injecting this optimality condition into a steepest  
 581 descent algorithm, an update of the forcing at an iteration  $n$  reads:

$$582 \quad f_\epsilon^{n+1} = f_\epsilon^n - \lambda \left. \frac{\partial \mathcal{L}^{H^1}}{\partial f_\epsilon} \right|_n, \quad (3.7)$$

583 in which the step size is constrained by  $\lambda = \beta \frac{1}{\max(\frac{\partial \mathcal{L}^{H^1}}{\partial f_\epsilon})}$  where  $\beta = 2 \cdot 10^{-2}$  is chosen based  
 585 on the sensitivity validation. In the next section, we present some numerical results obtained

586 on a realistic case study in terms of the turbulence model parameters estimation and in terms  
 587 of their sensitivity analysis, with the objective of analysing the closure hypotheses of a given  
 588 RANS model using the data assimilation framework.

#### 589 4. Case study

590 In this section, we first describe the wind tunnel experiments. Then, we present the numerical  
 591 setup.

##### 592 4.1. Description of the wind tunnel experiment

593 Experimental data were provided by the CSTB (Nantes, France) from the work of Sheng *et al.*  
 594 (2018). Measurements were performed in the atmospheric wind tunnel (NSA) with a test  
 595 section of 20 m long, 4 m wide and 2 m high. Upstream of the isolated building, roughness  
 596 elements and turbulence generator were set to reproduce the wind profile perceived by the  
 597 full scale building. The floor of the wind tunnel is equipped with a turntable that enables  
 598 the flow incidence to vary from 0 to 360°. In the present paper, only one wind direction is  
 599 considered. In these experiments, the building was modeled with a wall-mounted prism of  
 600 square cross-section with the dimensions: 10 cm × 10 cm × 49 cm which corresponds to a  
 601 tower of height  $H = 147$  m and a width  $D = 30$  m at full scale. To perform measurements,  
 602 two tower models were built. The first model was made of Plexiglas which allows for optical  
 603 access and, thus, to use particle image velocimetry (PIV). The second model was equipped  
 604 with 265 pressure taps to measure the unsteady pressure distribution on the modeled building.

##### 605 4.2. Numerical setup

606 The open source library OpenFOAM (Jasak 1996) was used to implement the CFD and  
 607 adjoint governing equations. The library utilizes a second order finite volume discretisation  
 608 approach (Moukalled *et al.* 2016) and a fully implicit first order method for time integration.  
 609 A prediction-correction procedure is used for the pressure-velocity coupling based on the  
 610 Rhie-Chow interpolation (Rhie & Chow 1983). Correction for mesh non orthogonality was  
 611 applied for the Poisson solver. A full scale building is modeled and a neutral atmospheric  
 612 boundary model was used (Richards & Hoxey 1993) to enforce the inlet wind profiles.  
 613 Profiles for  $U$ ,  $k$  and  $\epsilon$  are defined as

$$614 \quad U_{in} = \frac{u_{\tau}^{ABL} \ln\left(\frac{z+z_0}{z_0}\right)}{\kappa}, \quad k_{in} = \left(\frac{u_{\tau}^{ABL}}{C_{\mu}}\right)^2 \quad \text{and} \quad \epsilon_{in} = \frac{(u_{\tau}^{ABL})^3}{\kappa(z+z_0)}, \quad (4.1)$$

615 where  $u_{\tau}^{ABL}$  is the friction velocity associated with the constant shear stress along the ABL  
 616 width

$$617 \quad u_{\tau}^{ABL} = \frac{\kappa U_{ref}}{\ln\left(\frac{H_{ref}+z_0}{z_0}\right)}$$

618 in which  $U_{ref}$  and  $H_{ref} = \frac{2}{3}H$  are, respectively, reference velocity and height chosen to  
 619 match with the experimental profiles (and thus the eurocode (EN 2005)) (see figure 3). These  
 620 profiles are consistent with the wall treatment as we prescribes eddy viscosity's ground-value  
 621 by (2.40), such that  $u_{\tau} = u_{\tau}^{ABL}$ . As for the roughness height  $z_0$ , it was set to 0.02, as an  
 622 intermediate between the roughness class I and class II (EN 2005).

623 The size of the computational domain was fixed to ensure that the blockage effects are  
 624 inferior to 3% (Tominaga *et al.* 2008; EN 2005). Grid refinement was chosen to ensure a  
 625 good representation of the wind gradient at the inlet. Unstructured grid was then adopted

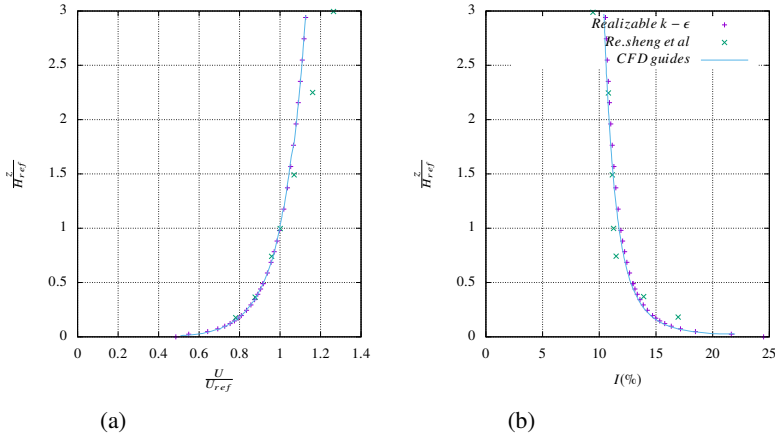


Figure 3: Profile of the neutral atmospheric boundary layer: (a), mean wind velocity; (b), turbulent intensity  $I$  as defined in (EN 2005).

626 with the minimum distance of the centroid of the cell adjacent to the building walls set to  
 627  $0.001 H$ . This grid refinement reached approximately 3.5 million cells.

628 The adjoint differential equations were discretised using the same CFD library as for the  
 629 direct equations. As for the direct simulation, the adjoint pressure and velocity were iteratively  
 630 solved using a prediction-correction procedure. The discretisation schemes used for the flow  
 631 equations were maintained. Moreover, we note that the derivation of the non-linear terms  
 632 leads to an explicit dependency of the adjoint solution on the direct flow solutions that  
 633 prevents a parallel computation of the two solvers.

## 634 5. Results

635 In this section, we validate the proposed data assimilation scheme for global and distributed  
 636 turbulence model parameters. An adjoint state analysis is conducted to obtain the sensitivities  
 637 to both model control closure parameters, global and distributed coefficients. We assess the  
 638 limits of global closure optimization performances and exhibit the ability of the proposed  
 639 distributed closure method not only to reconstruct wall-pressure-driven wake flow accurately  
 640 but also to enable turbulence closure analysis.

641

### 5.1. Adjoint state analysis

642 The normalised adjoint fields (by their maximum in-plane values), shown in figures 4, 5 and 6,  
 643 highlight the areas of interest in terms of turbulence modelling on two horizontal plans (at  
 644 normalised height  $z/H_{ref} = \{0.19, 1\}$ ) and on the symmetry plan (at  $y/D = 0$ ). These areas  
 645 correspond to regions, whose state is observable by the sensors, and where the turbulence  
 646 closure model fails to reproduce the physical behaviour of the flow; this corresponds to the  
 647 recirculation regions behind and at the top of the building (as seen in the centered streamwise  
 648 vertical plans on figure 6), the area of the vortex shedding due to flow separation (seen in  
 649 the horizontal plans on figure 4 and 5) and the flow impingement region of the building.  
 650 Based on these adjoint fields, the cost functional's sensitivity to any control parameter (be  
 651 distributed or not) can be obtained through its associated optimality condition.

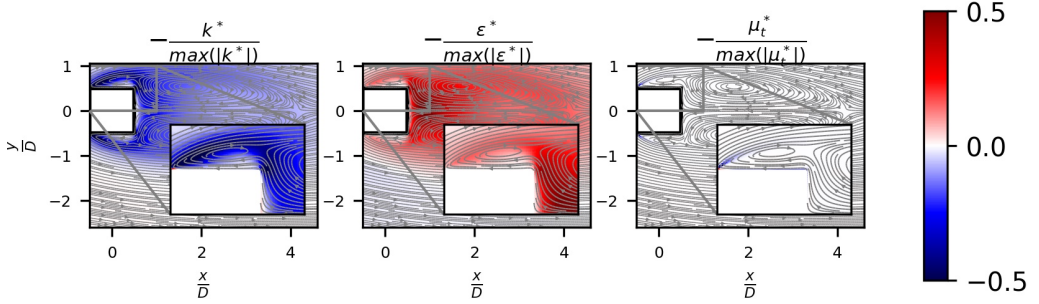


Figure 4: Adjoint turbulence variables at horizontal plan with normalised height  $z/H_{ref} = 0.19$ :(a),  $\epsilon^*$ ; (b),  $k^*$ ; (c),  $\mu_t^*$ . Variables are normalised by their in-plan peak values.

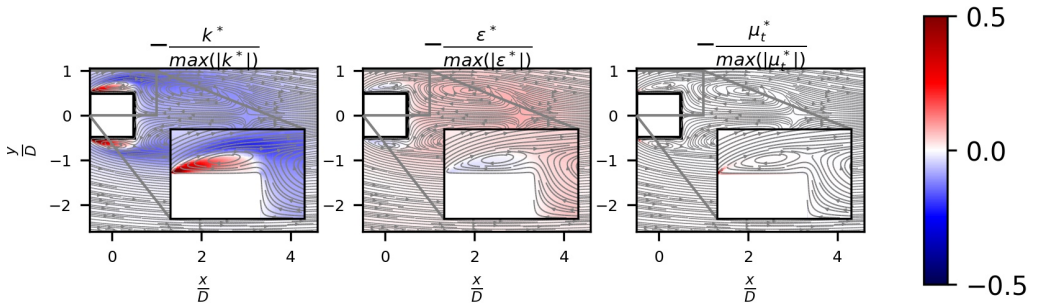


Figure 5: Adjoint turbulence variables at horizontal plan with normalised height  $z/H_{ref} = 1$ :(a),  $\epsilon^*$ ; (b),  $k^*$ ; (c),  $\mu_t^*$ . Variables are normalised by their in-plan peak values.

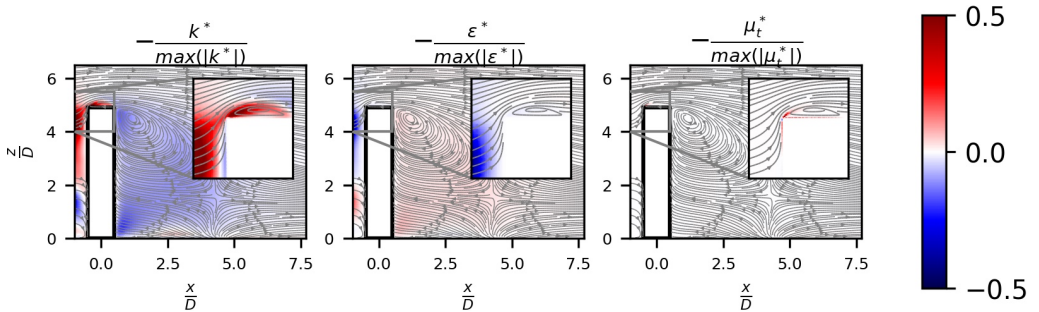


Figure 6: Adjoint turbulence variables at symmetry plan :(a),  $\epsilon^*$ ; (b),  $k^*$ ; (c),  $\mu_t^*$ . Variables are normalised by their in-plan peak values.

652

## 5.2. Results for the global coefficients

653 This section exhibits the adjoint approach's capability to provide a complete information  
 654 on the cost sensitivity to the model's global coefficients. First, we analyse the sensitivity  
 655 fields to highlight the spatial locations where a modification of these global coefficients  
 656 could efficiently correct the model errors. Then, we discuss the results of a data assimilation  
 657 procedure. The data assimilation is performed to investigate some closure hypotheses validity  
 658 in the RANS modelling.

---

	$\frac{\partial \mathcal{J}}{\partial A_0} (\times 10^7)$	$\frac{\partial \mathcal{J}}{\partial \sigma_k} (\times 10^7)$	$\frac{\partial \mathcal{J}}{\partial \sigma_\epsilon} (\times 10^7)$	$\frac{\partial \mathcal{J}}{\partial C_2} (\times 10^7)$
AD	1.371	-2.756	0.712	-8.583
FD ( $\delta\alpha_i = 10^{-1}$ )	2.39	-3.11	0.683	-6.699
FD ( $\delta\alpha_i = 10^{-2}$ )	2.07	-3.76	0.77	-11.4
FD ( $\delta\alpha_i = 10^{-3}$ )	2.05	-3.04	-	-11.9

---

Table 1: Sensitivity derivative values computed from the proposed adjoint model (AD) and the finite difference (FD).

---

### 659 5.2.1. Sensitivity analysis

660 First, a validation test has to be done to check the validity of the sensitivity fields. To that  
661 end, a specific innerproduct is employed in the variational formulation by considering an  
662 integration over a volume of interest, where the sensitivities are the most important. This  
663 volume of interest,  $\Omega_{in}$ , is centred around the building and has a size of  $2.5H \times 4H \times 1.5H$ .  
664 It is introduced in equation (2.15), and used to compute the optimality condition through the  
665 following weighted sum

$$666 \quad \left. \frac{\partial \mathcal{J}}{\partial \alpha_i} \right|_{AD} = \left\langle \frac{\partial \mathcal{M}}{\partial \alpha_i}, \mathbf{X}^* \right\rangle_{\Omega_{in}} \equiv \sum_j^{\text{nCells}} \left( \frac{\partial \mathcal{M}}{\partial \alpha_i} \cdot \mathbf{X}^* \right) \omega_j,$$

667 where  $\omega_j$  denotes the volume of the  $j^{\text{th}}$  cell. The validation metric is chosen to be the error  
668 between this weighted sum and the finite difference gradient computed by the cost function  
669 variations resulting from a small variation of the global coefficients in the volume of interest,

$$670 \quad \left. \frac{\partial \mathcal{J}}{\partial \alpha_i} \right|_{FD} = \frac{(\mathcal{J}(\alpha_i + \delta\alpha_i) - \mathcal{J}(\alpha_i))}{\delta\alpha_i}.$$

671 The sensitivity (gradient) of  $\mathcal{J}$  with respect to the four closure coefficients computed using  
672 the proposed adjoint approach and the finite differences are given in table 1. The comparison  
673 shows that the adjoint-based sensitivities are very close to the finite difference values. A  
674 fair agreement is obtained for the sensitivity associated with the coefficients involved in the  
675 redistribution of  $k$  and  $\epsilon$ . However, deviations appear to be notably more important for the  
676 eddy viscosity pre-factor  $A_0$ . These deviations are typical of the error levels associated to  
677 continuous adjoint methods. (Othmer 2008; Zymaris *et al.* 2010). This validates hence the  
678 procedure.

679 In order to explore the effect of the turbulence model's global coefficients, their associated  
680 sensitivity maps (plotted in figure 7, 8, and 9, and defined by the spatially distributed operand  
681 inside the integral in the optimality condition (3.1)) are discussed.

682 We can see there is high interest in optimising these coefficients at the shear layers resulting  
683 from flow separations at the leading lateral edges and on top of the building. However, there  
684 is very little sensitivity in the bulk of the recirculation wake region. Moreover, with regards  
685 to the regularity of the sensitivity fields,  $\frac{\partial \mathcal{J}}{\partial \sigma_k}$  and  $\frac{\partial \mathcal{J}}{\partial \sigma_\epsilon}$  (Figures 7 and 8 (a) and (b))  
686 have the largest local variations compared to the others. In fact, this is explained by the  
687 high (second) order derivative associated with the diffusion of  $k$  and  $\epsilon$ , in the optimality  
688 conditions. Now, regarding the local signs and overall values of each sensitivity field, we  
689 observe systematic change of sign over the domain. The  $L^2$  inner product in (3.1) leads to  
690 an averaged compromise solution over the whole domain for the global coefficient values.  
691 This compromise is likely to provide a far too weak amplitude for these coefficients in key  
692 regions of the flow.



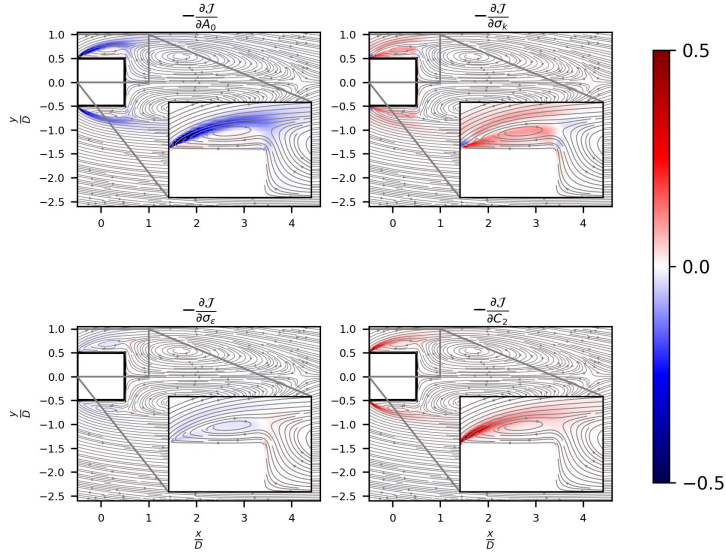


Figure 7: Closure coefficient sensitivities at horizontal plan with normalised height  $z/H_{ref} = 0.19$ : (a), sensitivity to  $A_0$ , (b),  $\sigma_k$ ,  $\sigma_\epsilon$  (c), and, (d),  $C_2$  (d). Sensitivities are normalised by their in-plan peak values.

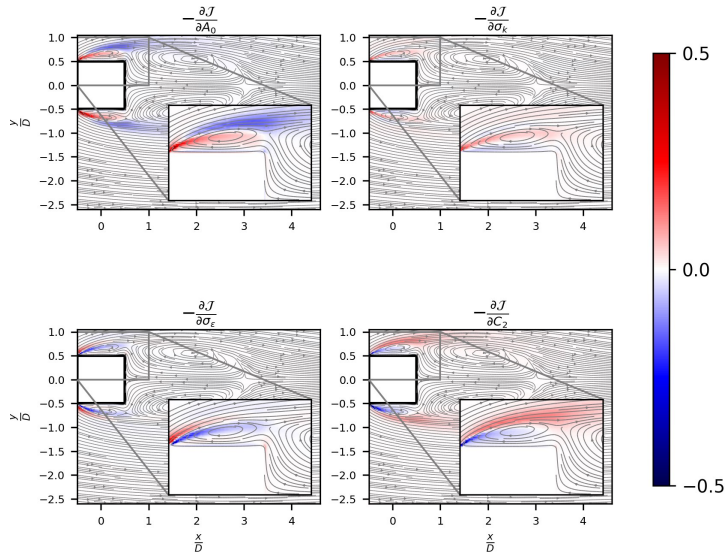


Figure 8: Closure coefficient sensitivities at horizontal plan with normalised height  $z/H_{ref} = 1$ : (a), sensitivity to  $A_0$ , (b),  $\sigma_k$ ,  $\sigma_\epsilon$  (c), and, (d),  $C_2$  (d). Sensitivities are normalised by their in-plan peak values.

693 As shown in table 1,  $C_2$  is the most sensitive coefficient. Its large value suggests that the  
 694 coefficient is less subject to sign cancellations in the sensitivity maps. This is especially  
 695 observed in the horizontal map at lower elevations far enough from the high-end (plot at  
 696  $z/H_{ref} = 0.19$  where  $H_{ref} = 2/3H = 3.3D$ ). With regards the other coefficients, their  
 697 global sensitivity derivatives suggest, a decrease of both the eddy-viscosity pre-factor  $A_0$ , the  
 698 turbulent energy diffusivity pre-factor  $1/\sigma_k$  and an increase of the diffusivity pre-factor  $1/\sigma_\epsilon$   
 699 of the energy dissipation. This implies, in the one hand, that the turbulence dissipation rate

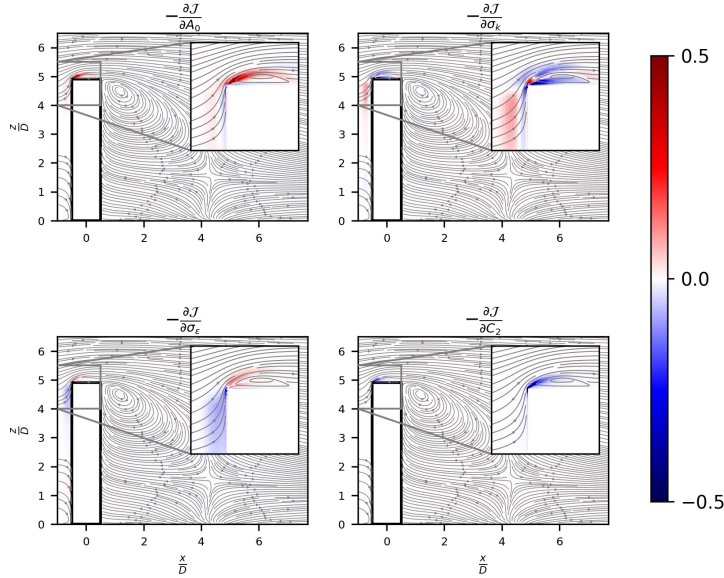


Figure 9: Closure coefficient sensitivities on the symmetry plan with normalised: (a), sensitivity to  $A_0$ , (b),  $\sigma_k$ ,  $\sigma_\epsilon$  (c), and, (d),  $C_2$  (d). Sensitivities are normalised by their in-plan peak values.

700 is under-predicted all over the domain and that a better redistribution of the flow field can be  
 701 obtained by increasing  $C_2$ . Inversely, by decreasing the eddy viscosity pre-factor  $A_0$  (which  
 702 increases  $C_\mu$ ), this trend shows that the original turbulence model tends globally to under-  
 703 estimates the momentum mixing and thus it globally advocates higher turbulent diffusion. By  
 704 looking at local sensitivities to this coefficients, these global directions are strongly driven  
 705 by the high interest giving to the lateral free-stream (surrounding lateral recirculating flow)  
 706 entrained toward the wake region. Thus, upon calibration, we may expect some preferential  
 707 improvement of the wake extension and, inversely, a retrogression in the extension of lateral  
 708 separated flow.

### 709 5.2.2. Closure hypothesis analysis through data assimilation

710 In this section, the optimisation problem is solved iteratively by following Algorithm 1, and  
 711 we discuss the data assimilation procedure's ability to estimate the flow state. Guided by the  
 712 work of Shih *et al.* (1995), we intend here to devise some penalty ranges for the coefficients.  
 713 Concerning the coefficients which are involved in the energy dissipation rate budget, referring  
 714 to the work (Shih *et al.* 1995), the  $C_2$  coefficient is actually expressed as  $C_2 = \beta/\eta$ , in which  
 715  $\beta = \eta + 1$  is the dissipation decay rate (such as  $\epsilon/\epsilon_{t_0} = (t/t_0)^{-\beta}$  where  $t_0$  is an initial time)  
 716 and  $\eta$  is the energy decay exponent (such as  $k/k_{t_0} = (t/t_0)^{-\eta}$ ) that varies from 1.08 to 1.3  
 717 in decaying homogeneous turbulence experiments (Shih *et al.* 1995). Thus, a range for this  
 718 coefficient can be set as  $C_2 \in [1.76, 1.93]$ , where the background value is 1.9.  
 719 For  $\sigma_\epsilon$ , the inertial turbulence assumption near the wall allows to establish

$$720 \quad \sigma_\epsilon = \frac{\kappa^2}{C_2 \sqrt{C_\mu} - C_1} \quad (5.1)$$

721 were the von Kármán constant  $\kappa = 0,41$ , the eddy viscosity coefficient  $C_\mu = 0.09$  and  
 722  $C_1 = 0.43$ . Assuming a quasi-linear dependency between the two constants (see figure 11),  
 723 knowing the range on  $C_2$  we obtain  $\sigma_\epsilon \in [1.14, 1.71]$ . To possibly relax the underlying



---

Scenario	$\sigma_k$	$\sigma_\epsilon$	$C_2$	$A_0$	$\frac{\mathcal{J}-\mathcal{J}_0}{\mathcal{J}_0}$
Default value	1.0	1.2	1.9	4.0	
<b>A</b>	1.14	0.99	1.92	4.05	10.7%
<b>B</b>	1.0	0.74	1.96	4.08	15.7%
<b>C</b>	1.03	1.07	1.95	3.99	9.8%

---

Table 2: Summary of the optimisation results, closure coefficients and the relative decrease of cost function.

---

724 assumption of decaying turbulence for this range, two cases study will be considered for this  
725 constant. In the first scenario, it will be assumed that relation (5.1) holds beyond the inertial  
726 layer, as established by Shih *et al.* (1995). On the second scenario, this constraint is relaxed  
727 and coefficient  $\sigma_\epsilon$  is assumed to be an independent control parameter. In that case, the closure  
728 is thus performed by the data. The second case is expected to bring more degree of freedom  
729 in the optimisation process, due to the independent adaptation of the two coefficients.

730 In the transport equation of  $k$ , the coefficient  $\sigma_k$ , which adjusts the level of turbulent energy  
731 mixing with respect to the momentum eddy diffusivity, is in commonly fixed to unity (as in  
732 any  $k - \epsilon$  turbulent model). This generally assumes a quasi-equality between the scalar and  
733 the momentum mixing. Due to the lack of comparative studies in the literature between the  
734 *realizable* model results and experiments, estimating a physical range for this coefficient is  
735 not possible. Therefore, we considered two optimisation procedures where in the first one  
736 we maintain  $\sigma_k = 1$  while in the other case we relax this constraint letting  $\sigma_k$  evolves in the  
737 arbitrary chosen range:  $\sigma_k \in [0.9, 1.1]$ . Similarly, for the bounds on  $A_0$ , without any *a priori*  
738 informations on its physical range, we fixed a larger range of possible value:  $A_0 \in [3.6, 4.4]$ ,  
739 where the background usual value is 4.0.

740 Based on the remarks of the previous section, the results of three data-assimilation  
741 scenarios are discussed and compared. A first straightforward approach corresponds to the  
742 optimisation of the four coefficients independently. This is referred to as scenario **A**. Then, two  
743 scenarios are considered to investigate the two closure assumptions mentioned in the previous  
744 section. First, we consider the equality between the mixing of turbulent kinetic energy and  
745 momentum, referred as scenario **B**. Secondly, keeping  $\sigma_k$  a free parameter, the scenario **C**  
746 consists in enforcing the inertial constraint and defining  $\sigma_\epsilon$  using (5.1). Three criteria are  
747 considered to evaluate the agreement between the CFD results and the measurements. The  
748 first is the relative reduction of cost function  $\frac{\mathcal{J}-\mathcal{J}_0}{\mathcal{J}_0}$ ,  $\mathcal{J}_0$  being the initial cost. This depicts  
749 the improvement of the global effect of wind on the building. Next,  $C_p$ , the dimensionless  
750 pressure, is compared locally on the facades of the building. Third, to quantify the accuracy  
751 of the recovered mean flow field, the streamwise length of the recirculation region behind  
752 the building is compared to the one observed from the PIV plans.

753 Regarding the update of the coefficients, a steepest descent algorithm is used with an adaptive  
754 step. A maximum step size is set to  $10^{-2}$  while a minimum step size inferior to  $10^{-4}$  is  
755 considered as an optimisation convergence criteria. The confidence coefficients are all set  
756 to  $\zeta_i = 5 \times 10^{-2}$ . This low uniform values represent a relative degree of confidence on the  
757 background closure values. The variations of the closure coefficients along the optimisation  
758 iterations are shown in figure 10. The maximum reduction of the cost and the optimal  
759 coefficients values for the three considered scenarios are summarised in table 2. In terms  
760 of mismatch between CFD and experimental mean pressure, it is shown that the highest  
761 reduction can be achieved through the optimisation scenario **B**. Conversely, scenario **C** leads  
762 to the least improvement in the cost function. However, we note a faster convergence rate for

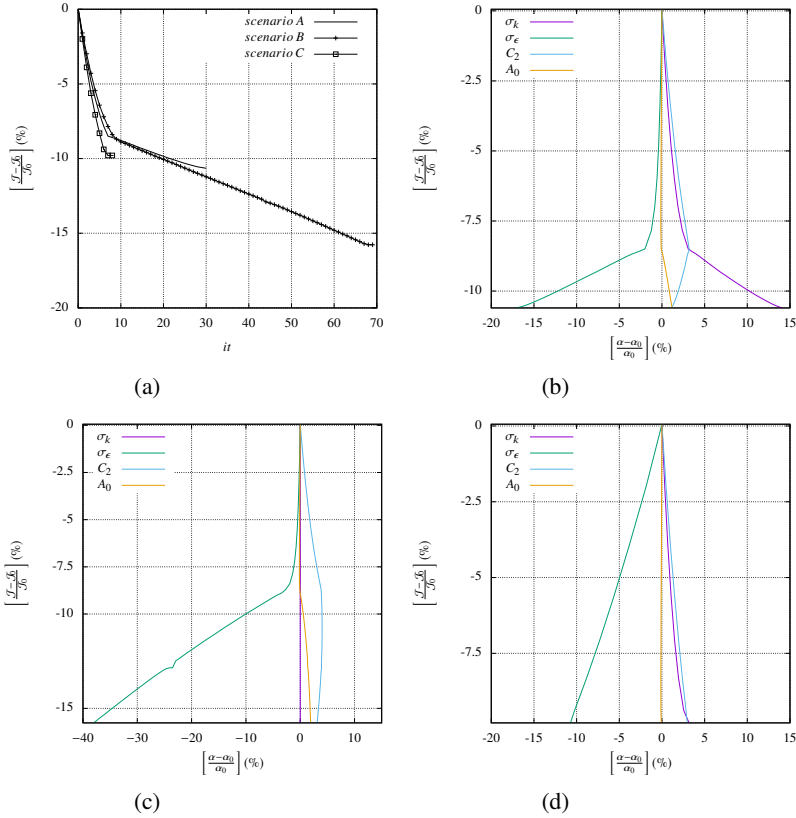


Figure 10: Cost function reduction, (a), and closure coefficient variations: (b), scenario **A**; (c), scenario **B**; (d), scenario **C**.

763 **C**, for which the optimal solution is reached 10 times faster than for **B**. Furthermore, a shift  
 764 between the two regimes can be noticed in scenarios **A** and **B**. Indeed, this shifting occurs  
 765 when the penalisation on the variation of  $C_2$  becomes of the same order of magnitude than the  
 766 required advancement for the cost minimisation. Whereas in **B**,  $\sigma_k$  is not optimised and the  
 767 trend on  $C_2$  until convergence is mainly dominated by its penalisation. In all scenarios, the  
 768 optimal value of  $C_2$  increases while it stays within 5% of the background value. Considering  
 769  $A_0$ , a minor variation is observed during optimisation in all scenarios. On the contrary, a  
 770 higher variation of  $\sigma_\epsilon$  below the recommended range is necessary to reduce the cost function.  
 771 In figure 11, we show the variation of  $\sigma_\epsilon$  with respect to  $C_2$ . In scenario **C**, a quasi-linear  
 772 dependency is established through relation (5.1). However, we retrieve the two regimes in **B**  
 773 and **A** where this dependency is broken.

774 In general, it can be concluded that a better agreement between the turbulence model (e.g  
 775 *realizable*  $k - \epsilon$ ) and wind tunnel experiments, in terms of wind load on the facades of  
 776 high-rise buildings, can be achieved through optimisation of the closure coefficients. Even  
 777 if it offers less degrees of freedom in the optimisation, better results are obtained when  
 778 enforcing the constraint that equals turbulence mixing in the equation of transport of  $k$  to  
 779 momentum mixing by the eddy viscosity (scenario **B**). This suggests that it is a physically  
 780 valid hypothesis in our case study. It helps structuring the data assimilation process and  
 781 leads to a robust procedure. It states that the turbulent mixing of the momentum and kinetic  
 782 energy are of same nature. At the opposite, by relaxing the constraint and establishing

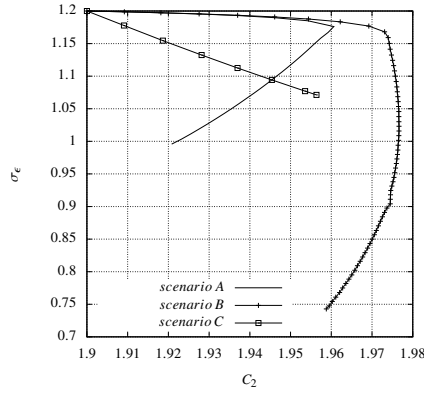


Figure 11:  $\sigma_\epsilon$  variations with respect to  $C_2$  for all scenarios.

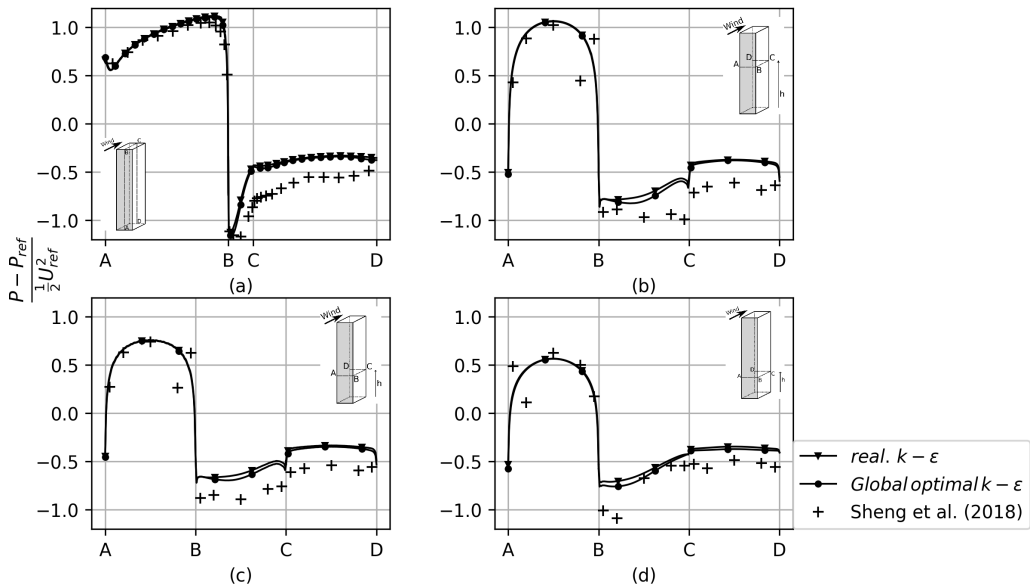


Figure 12: Comparison of pressure coefficient profiles between CFD (scenario **B**) and experimental results along building facades. Contours are taken at building symmetry plan, (a) and three horizontal plans at  $z/H_{ref} = 1$ , (b),  $z/H_{ref} = 0.27$ , (c) and  $z/H_{ref} = 0.19$ , (d), respectively.

783 relation (5.1) as valid out of the inertial layer (scenario **C**) may lead to lower agreement  
 784 with measurements. Indeed, this assumption may hold reasonably in flows where turbulence  
 785 behaviour is isotropic. However, in the presence of bluff body, e.g flows with separation  
 786 and recirculation dynamics, this assumption is undoubtedly unrealistic. Scenario **B** might  
 787 be considered as the best optimisation choice to get better wind load representation on high-rise  
 788 building given the considered turbulence closure (*i.e.* realizable  $k - \epsilon$ ). Following the best  
 789 optimisation scenario, 15% gain on the overall predicted loads are obtained. Furthermore, a  
 790 comparison of the predicted pressure coefficient at the building facades (see figure 12) this  
 791 gain is associated to the slight improvement observed especially along the side facades.

792 Nearly no change at the front facade and along the upfront corners is observed. As a matter  
 793 of fact, this observations confirms what was earlier mentioned in the sensitivity analysis

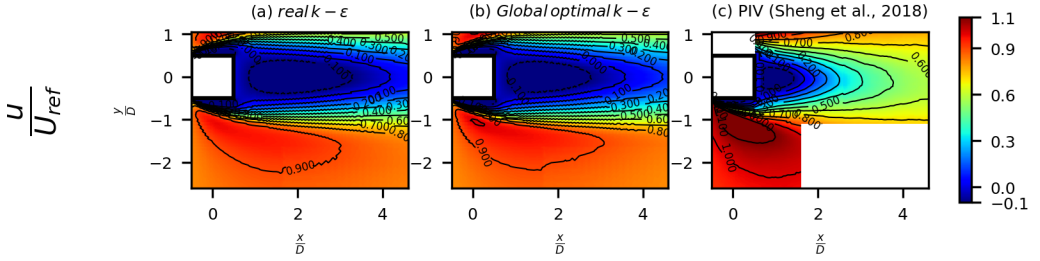


Figure 13: Comparison of mean stream-wise contour between CFD (scenario **B**) and Re. Sheng (PIV) experiments at horizontal plan with normalised height  $\frac{z}{H_{ref}} = 0.19$ .

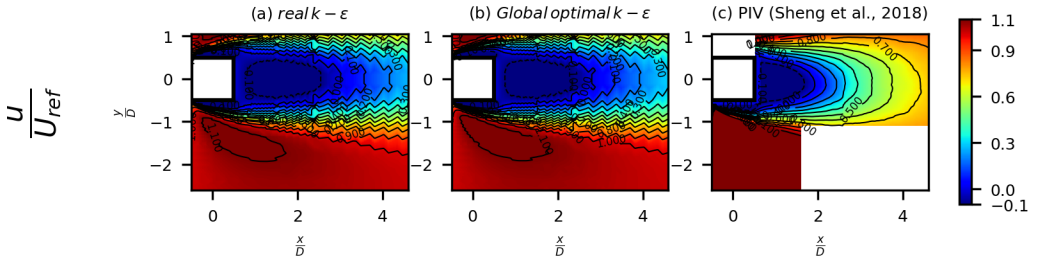


Figure 14: Comparison of mean stream-wise contour between CFD (scenario **B**) and Re. Sheng (PIV) experiments at horizontal plan with normalised height  $\frac{z}{H_{ref}} = 1$ .

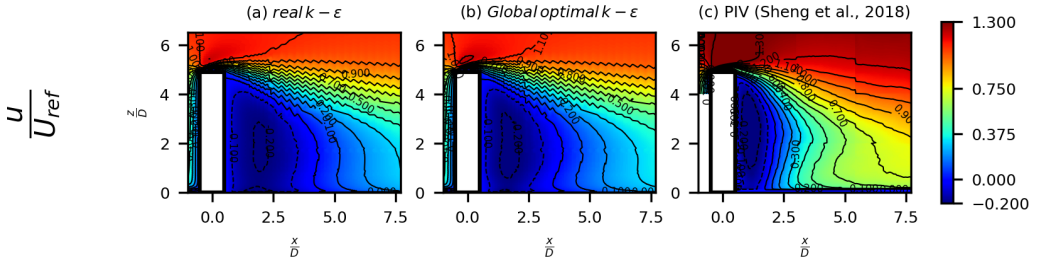


Figure 15: Comparison of mean stream-wise contour between CFD (scenario **B**) and Re. Sheng (PIV) experiments at symmetry plan with normalised height  $\frac{z}{H_{ref}} = 1$ .

794 where the rigidity of the considered turbulence model is shown to play a major role on the  
795 degree of improvement that can be achieved to fit with measurements.

796 With regard to the mean flow reconstruction, adopting the best optimisation scenario  
797 (scenario **B**), the contours of the mean velocity field are compared with the available PIV  
798 plans reported from the work of Sheng *et al.* (2018). It is a strong validation since these  
799 measurements are not used in the data assimilation. Figures 13, 14 and 15 show the normalised  
800 streamwise velocity at the streamwise central plan (top) and at two horizontal plans, *i.e.*  
801  $z/H_{ref} = 0.19$  and  $z/H_{ref} = 1$ . The CFD with background values and optimised values  
802 following **B** are compared with the PIV measurements.

803 In order to show the effect of data assimilation, velocity contours are superimposed  
804 (right column) and thicker lines are plotted to track the size of the recirculation region.  
805 The reattachment length on the ground, is reported in table 3. After optimisation, velocity  
806 contours show a better estimation of the recirculation region length which is shorter compared  
807 to the non-optimised model. This improvement is more affirmed near the ground, where the  
808 relative error of reattachment length  $Y$  with respect to PIV,  $\varepsilon_Y = \frac{\nabla Y_0}{\nabla Y_{end}}$ , with the default

---

	<i>Exp realizable <math>k - \epsilon</math> optimised</i>		
$Y^f(m)$	$\sim 50$	139.8	117.1
$Y^r(m)$	-	13.6	11.7

---

Table 3: Comparison of the (dimensional) reattachment lengths on the roof and floor, CFD optimised with global constant calibration (scenario **B**).

---



---

	$\frac{\partial \mathcal{J}}{\partial f_\epsilon} (\times 10^8)$
AD	-3.55
FD ( $\delta f_\epsilon = 10^{-1}$ )	-14.03
FD ( $\delta f_\epsilon = 10^{-2}$ )	-4.03
FD ( $\delta f_\epsilon = 10^{-3}$ )	-4.45
FD ( $\delta f_\epsilon = 10^{-4}$ )	-4.43
FD ( $\delta f_\epsilon = 10^{-5}$ )	-4.19

---

Table 4: Sensitivity derivative w.r.t.  $f_\epsilon$  computed from the proposed adjoint model (AD) and the finite difference (FD) with different perturbation sizes.

---

809 ( $Y_0$ ) and the optimised ( $Y_{\text{end}}$ ), is reduced by 25%. Despite this enhancement, it should be  
810 pointed out that CFD model still under-predicts the flow in the wake region. This is the  
811 best improvement of this specific turbulence model we obtained by assimilating the pressure  
812 measurements. The two limiting ingredients are the model rigidity and the partial sparse  
813 observations (pressure at the boundary) of the complex flow. In the next section, spatially  
814 distributed control parameters in the transport equation of dissipation are considered in order  
815 to relax this structural constraint.

### 816 5.3. Distributed closure parameter in the energy dissipation budget

817 This section is dedicated to the results related to the investigation of the adjunction on  $k - \epsilon$   
818 (realizable) model of a distributed control parameter in the energy dissipation rate budget.  
819 First, we analyse the sensitivity fields to highlight the spatial locations where the closure  
820 form of  $\epsilon$  budget appears inadequate to reproduce the measurements and would require a  
821 structural correction. Then, the data-assimilation results of this spatially corrected model are  
822 analysed.

#### 823 5.3.1. Sensitivity analysis

824 For quantitative validation, adjoint sensitivities are compared with finite differences in table 4  
825 for different perturbations,  $\delta f_\epsilon = \{10^{-5}, \dots, 10^{-1}\}$  inside  $\Omega_{in}$  and zero elsewhere. Thus, the  
826 lower deviation obtained for a step size of  $10^{-2}$ , for which rounding errors are less effective,  
827 confirms the validity of the implementation.

828 We analyse the parameter sensitivity fields given by the proposed closure model, which  
829 corresponds to the first iteration step of the data assimilation procedure. Indeed, we are  
830 interested in the gradient of the cost functional with respect to the distributed control  
831 parameters for  $f_\epsilon = 0$ . Figures 16, 17, and 18 compare the sensitivity maps for the added  
832 control parameter against a direct forcing (which corresponds to the adjoint variable on  $\epsilon^*$ ).  
833 Globally, sensitivity to the proposed parameter  $f_\epsilon$  shows a strong response in a restricted  
834 flow area. In contrast with very diffused sensitivity maps for the direct forcing, the sensitivity  
835 maps of the additional forcing do highlight the regions of great relevance for the model

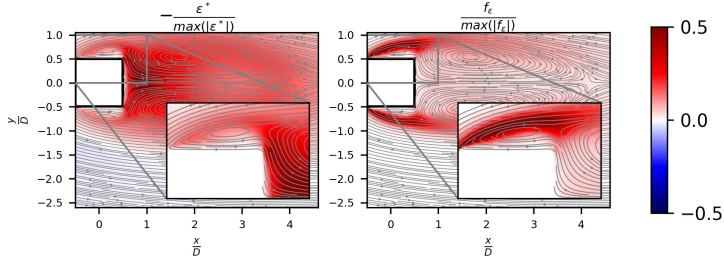


Figure 16: Adjoint turbulence dissipation and the constrained control at horizontal plan with normalised height  $\frac{z}{H_{ref}} = 0.19$ . Variables are normalised by their in-plan peak values.

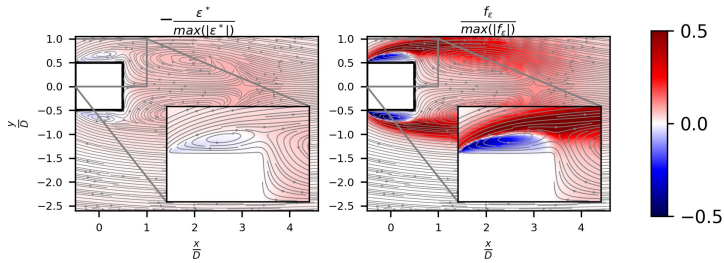


Figure 17: Adjoint turbulence dissipation and the constrained control at horizontal plan with normalised height  $\frac{z}{H_{ref}} = 1$ . Variables are normalised by their in-plan peak values.

836 improvement. They correspond to the same regions as those designated by the sensitivity  
 837 maps of the global constants in the previous section. For instance, we note a tendency to  
 838 bring significant dissipation rate adjustments starting from the leading edges and continuing  
 839 into the lateral shear layers and more downstream at the wake region edges. Let us note that  
 840 multiplication by the variable  $\epsilon$  has damped sensitivities at regions nonrelevant for turbulence  
 841 energy budget, such as the high peaks of sensitivity observed around the wake centerline  
 842 for the direct forcing (see figure 16). As we span upward, as shown at height  $z/H_{ref} = 1$   
 843 in figure 17, the maps actually reveal a step function tendency as we go from separated  
 844 flow regions, *i.e.*, the lateral and top shear layers, toward the wake region. Furthermore,  
 845 with regard to the sign, eventual contributions to the  $\epsilon$  budget are interpreted as follows.  
 846 A negative value of  $f_\epsilon$  would tend to increase the dissipation rate, while a positive value  
 847 would instead decrease it. Hence, on both lateral and top separated flows, the parameter  
 848 suggests there an increase of the dissipation rate. The sensitivity analysis points here an  
 849 over-production of turbulent kinetic energy, which is a known common default of the  $k - \epsilon$   
 850 closure models in such flow configurations reported, for instance, in (Murakami 1990, 1997;  
 851 Shirzadi *et al.* 2017). Moreover, along the outer edges of the lateral shears toward the wake  
 852 edges, the sensitivity maps suggest reducing the dissipation rate. This tendency is consistent  
 853 with a rather under-predicted turbulent mixing, resulting in the overly extended wake region  
 854 behind the building (Shirzadi *et al.* 2017).

### 855 5.3.2. Closure analysis through data-assimilation

856 We consider now the solution of a data-model coupling using the modified closure equation  
 857 (3.2). Regarding the assimilation procedure's setting, the steepest descent algorithm is used  
 858 with the Sobolev gradient computed in (3.6) as a descent direction. Regarding the filtering  
 859 choice, two values  $l_{sob} = 0.1D$  and  $0.2D$  were tested. Let us note that with  $l_{sob} = 0$ , *i.e.*  
 860 no smoothing of the  $L^2$  gradient, the procedure was notably unstable, showing the need for



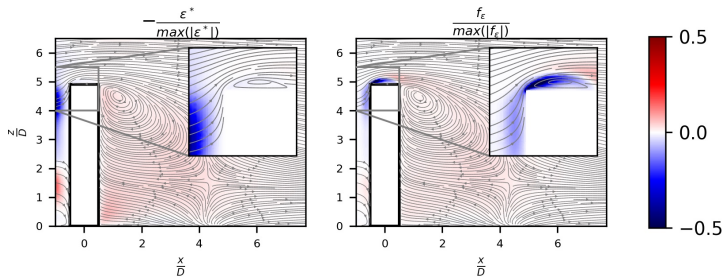


Figure 18: Adjoint turbulence dissipation and the constrained control at symmetry plan. Variables are normalised by their in-plan peak values.

861 regularisation. As for a higher value of  $l_{sob} = 0.2D = 6$  m, this choice yielded to an over  
 862 smoothing. As the sensitivity varies by length scales that are quite small in comparison to  
 863 this length, this advocates a value of  $l_{sob} \sim$  lateral recirculation width. Therefore, a filtering  
 864 length scale equivalent to 10% of the building's width seems to give a good compromise to  
 865 filter the small-scales, as suggested also in Tissot *et al.* (2020).

To assess the performance of the proposed regularisation technique, we compare the optimisation convergence using the Sobolev gradient with the cost penalisation approach. With an additional regularisation term given by the gradient of  $f_\epsilon$ , the cost function would read

$$\tilde{\mathcal{J}}(P, f_\epsilon) = \mathcal{J}(P) + \gamma \langle \nabla f_\epsilon, \nabla f_\epsilon \rangle_\Omega$$

in which  $\gamma = \zeta * \max(\epsilon \epsilon^*)$  is a free hyper-parameter controlling the amount of penalisation. Computing the Gateaux derivative w.r.t.  $f_\epsilon$  brings an additional volume term, such that the  $L^2$  optimality condition (3.4), which rewrites as

$$\frac{\partial \mathcal{L}}{\partial f_\epsilon} = \epsilon \epsilon^* - \gamma \nabla \cdot \nabla (f_\epsilon).$$

866 The comparison of the results obtained with both approaches are shown in figure (19)  
 867 for  $\zeta = 0.5, 1$ , and  $2.5$ . We can see that Sobolev gradient leads to the lowest discrepancy  
 868 ( $\frac{\mathcal{J}}{\mathcal{J}_0} \simeq 0.42$ ) compared to the best gradient penalisation ( $\frac{\mathcal{J}}{\mathcal{J}_0} \simeq 0.56$  with  $\zeta = 1$ ). Regarding the  
 869 convergence speed, minimisation with the Sobolev gradient reaches the minimum in less than  
 870 200 iterations while convergence for the regularisation approach with  $\zeta = 1$  requires more  
 871 than 400 iterations. The convergence process through the projection in  $H^1(\Omega)$  is therefore  
 872 much faster. This might come because adding the gradient to the cost function changes the  
 873 original descent direction prescribed by the discrepancy to data. Moreover, concerning the  
 874 calibration, the cost functional reduction has doubled compared to the calibration results  
 875 obtained using the best scenario  $\mathbf{B}$  ( $\frac{\mathcal{J}}{\mathcal{J}_0} \simeq 0.85$ ). Indeed, this difference is consistent because  
 876 the additive parameter  $f_\epsilon$  is less constrained by the parametric rigidity associated to the  
 877 global coefficients. In what follows, we analyse the method's performance in terms of the  
 878 flow reconstruction. This will further illustrate the adjoint approach's capability for data-  
 879 coupling with local corrections of the turbulence closure.

880 **Wind load profiles** The reconstructed pressure loads are compared with the experimental  
 881 data (Sheng *et al.* 2018) and the non-assimilated model in figure 20. We can see that, in  
 882 comparison with the coefficient calibration, the modified closure model produces far better  
 883 results in most of the building's wall regions. In terms of pressure discrepancy, the modified  
 884 closure model manages to capture well suction at both top leading edge in the symmetry  
 885 plan (point B in sub-figure(a)) and lateral leading edges (see figure 20(b), (c), and (d)).  
 886 However, while a good agreement with the data is obtained along the lateral facades, minor

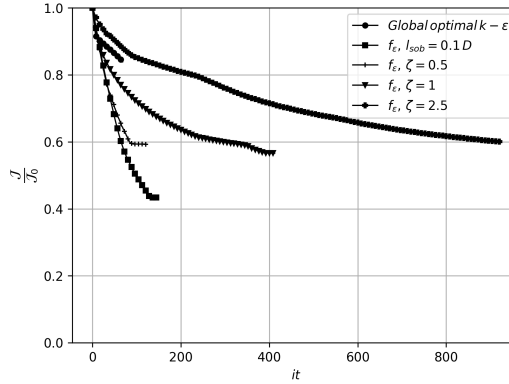


Figure 19: Cost function reduction. Comparison is made between an  $\epsilon$  budget correction and global calibration using scenario **B**.

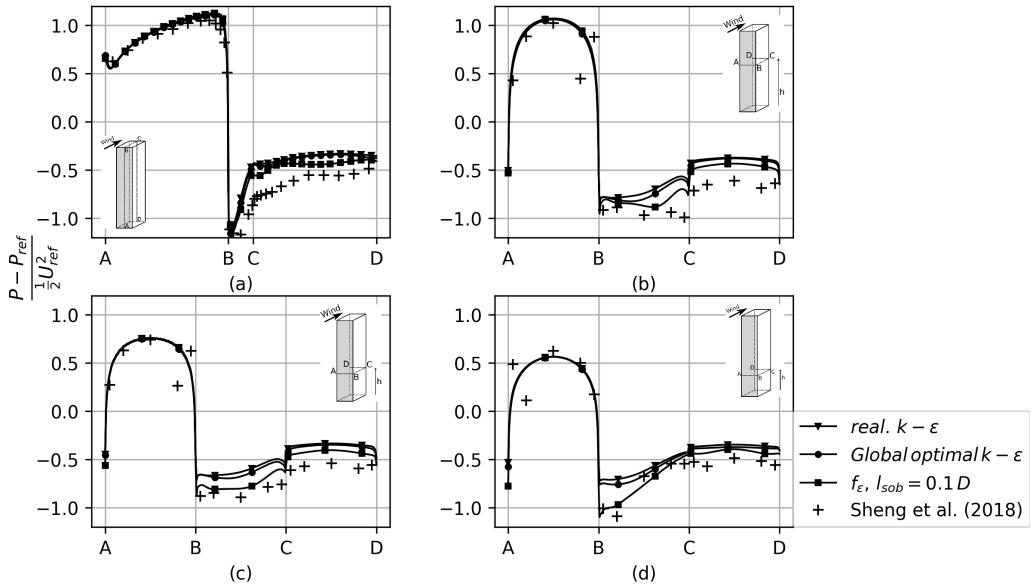


Figure 20: Pressure coefficient profiles along building facades. Comparison is made between an  $\epsilon$  budget correction and global calibration using scenario **B**. Contours are taken at building symmetry plan, (a) and three horizontal plans at  $z/H_{ref} = 1$ , (b),  $z/H_{ref} = 0.27$ , (c) and  $z/H_{ref} = 0.19$ , (d), respectively.

887 to important deviations are apparent as we get closer to the trailing edges and especially  
 888 when we approach the high-end. This gradually leads to poorer pressure interpolation as the  
 889 discrepancy reaches a maximum value at the upper back facade around  $H_{ref}$  (sub-figure(a)  
 890 and (b)). Yet, the modified closure model shows a slightly better prediction near the top-  
 891 trailing edge than the calibrated default model. Therefore, at this level of comparison, such  
 892 closure model does improve the data-model capability. The remaining regions where no  
 893 improvement is seen might reflect the limited controllability of such turbulence model with  
 894 wall pressure measurement.

895 **Flow topology** Regarding the spanwise flow structure, figures 21 and 22 show sectional  
 896 streamlines at both  $z/H_{ref} = 0.19$  and  $z/H_{ref} = 1$  height, respectively. Here it is noteworthy  
 897 to mention that these sectional streamlines are computed for in-plane velocity components.



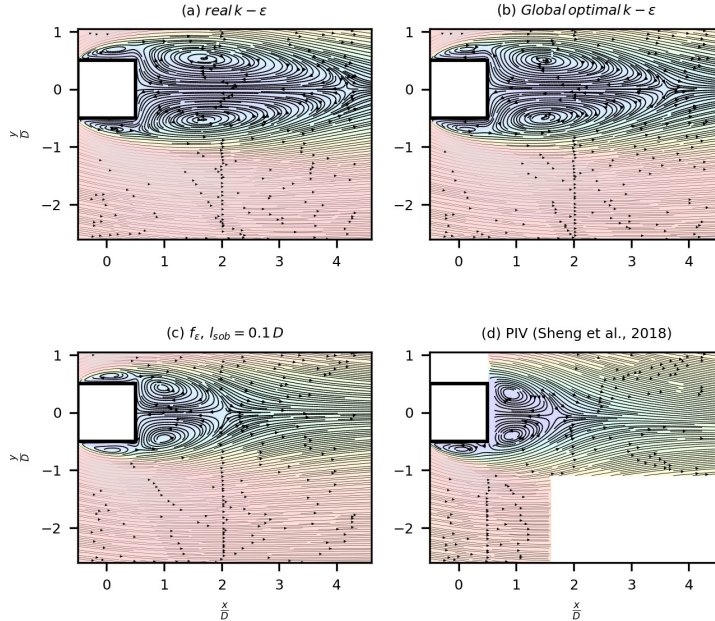


Figure 21: Flow topology (2D) on horizontal plan at normalised height  $\frac{z}{H_{ref}} = 0.19$  with local constraint correction. Comparison is made between an  $\epsilon$  budget correction and global calibration using scenario **B**.

898 In each sub-figure, streamlines predicted with the non-assimilated model (sub-figure (a)) is  
 899 compared with the calibrated model (scenario **B**) (b), with  $f_\epsilon$  closure correction (c) and PIV  
 900 experiments from Sheng *et al.* (2018) (d). At both levels, the model's reconstructed flow ( $f_\epsilon$ )  
 901 still preserves the symmetry of the two distinct pairs of averaged vortex structure. Moreover,  
 902 an excellent agreement with experiments is obtained in the wake transverse extension and  
 903 the vortices focal point positions in comparison with the calibrated model.

904 Figure 23 shows time-averaged sectional streamlines at the  $y/D = 0$  symmetry plane in  
 905 the transverse-wise structure. As can be seen from figure 23, the two distinct types of average  
 906 streamlines are also observed on both reconstructed flows ((b) and (c)). It is constituted by an  
 907 upper recirculation starting at the roof-top and a lower recirculation region raised from the  
 908 ground wall, separated by a saddle point. Thus, regarding the wake's extension, the modified  
 909 closure model leads to a drastic reduction of the recirculating flow compared to the calibrated  
 910 mode, thus reaching a realistic size. This can be quantified by the position of the saddle point  
 911 ( $x/D = 4, z/D = 2$ ) in the RANS model which has been moved around ( $x/D = 2, z/D = 2$ ).  
 912 This striking result is mitigated by the fact that this saddle point has been pulled slightly too  
 913 far upstream. It should be recalled that only pressure measurements in the facade have been  
 914 available and that PIV measurements are used here only for validation. This good agreement  
 915 with external data proves that we are neither in overfitting nor in an over-constrained situation.  
 916 Indeed, the two-dimensional vortices at both elevations ( $\frac{z}{H_{ref}} = 0.19, 1$ ) are a transverse  
 917 projections of the three-dimensional rolls, one on each side of the wake symmetry plan, which  
 918 connects near the free end. Such structure is consistent with some model descriptions brought  
 919 on wakes of finite length square cylinders, with similar height/width ratio, that are subject to  
 920 boundary layer flows of various thickness (Kawamura *et al.* 1984; Wang & Zhou 2009). A  
 921 global three-dimensional picture gathering the two-dimensional previous plots is shown in  
 922 figure 24). Examining the optimal forcing fields in figure 25, we retrieve the same tendencies

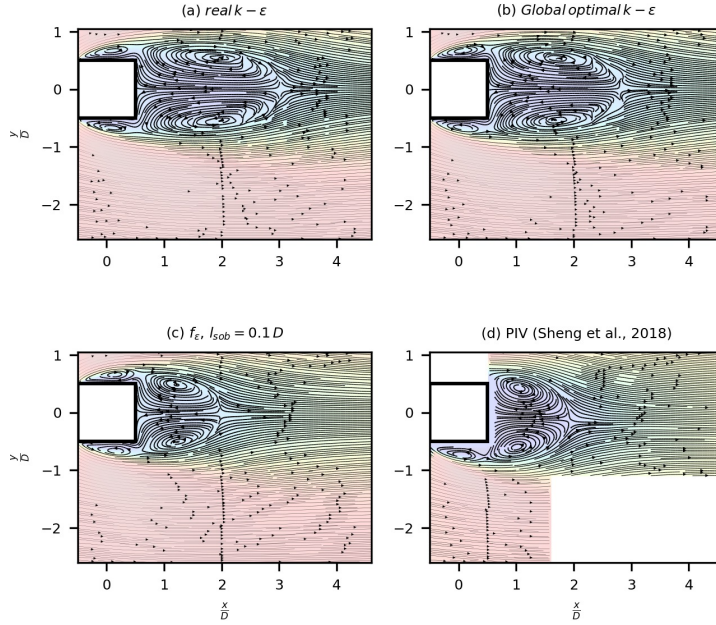


Figure 22: Flow topology (2D) on horizontal plan at normalised height  $\frac{z}{H_{ref}} = 1$  with local constraint correction. Comparison is made between an  $\epsilon$  budget correction and global calibration using scenario **B**.

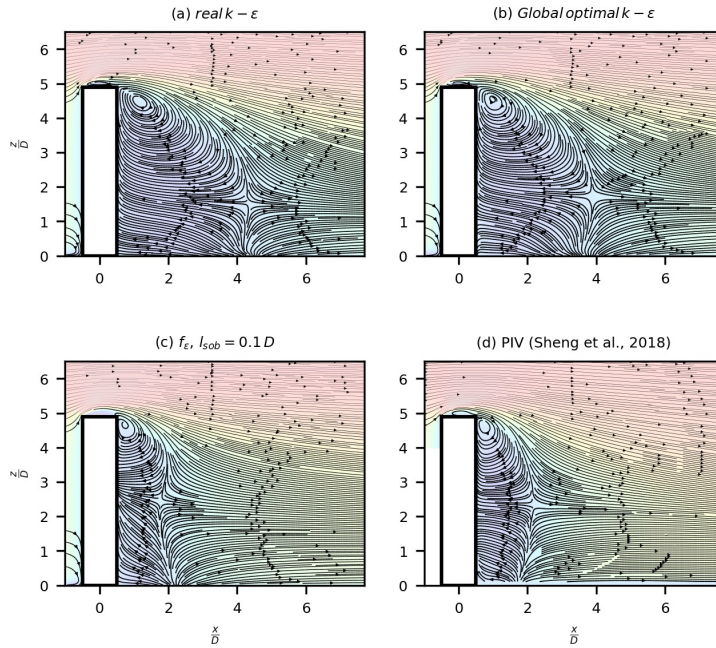


Figure 23: Flow topology (2D) on symmetry plan with local constraint correction. Comparison is made between an  $\epsilon$  budget correction and global calibration using scenario **B**.

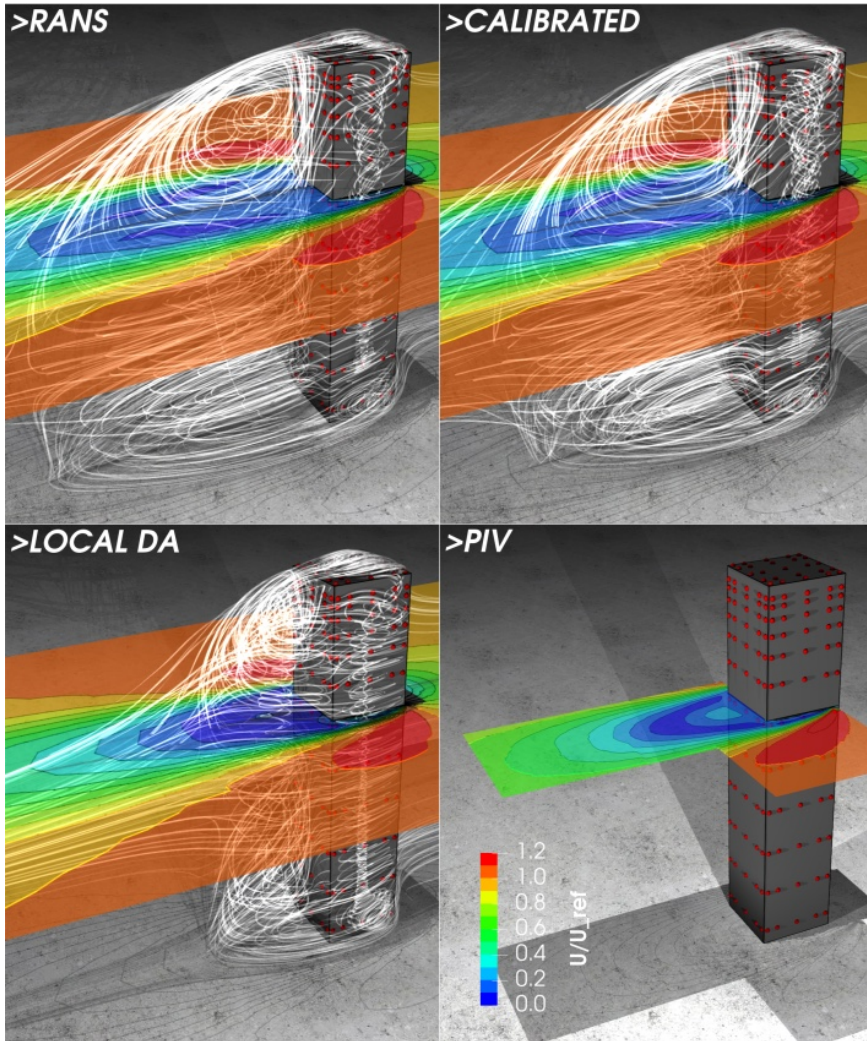


Figure 24: Flow topology (3D) of the realizable  $k - \epsilon$  model, global coefficient calibration and  $\epsilon$  budget correction against PIV plan at  $z/H_{ref} = 1$ .

923 observed in the sensitivity analysis before the reconstruction. After the optimisation, the  
 924 parameter  $f_\epsilon$  still keeps advocating less turbulence production into in the shear layers of the  
 925 lateral separated flow (see 25(a) and (b)), while, conversely, more mixing at the edges of the  
 926 wake downstream. Corrections are performed where strong turbulence inhomogeneity and  
 927 anisotropy occur. It acts in a way to redistribute dissipation rate, by the means of sources  
 928 and sinks, from the upstream region toward the downstream region. When considering only  
 929 calibration of the global coefficients, the model structure prevents this redistribution. This  
 930 suggests that some turbulence mechanisms related to anisotropy and inhomogeneity effects  
 931 are not properly taken into account in the model closure and need to be included to represent  
 932 accurately some key regions of the flow.



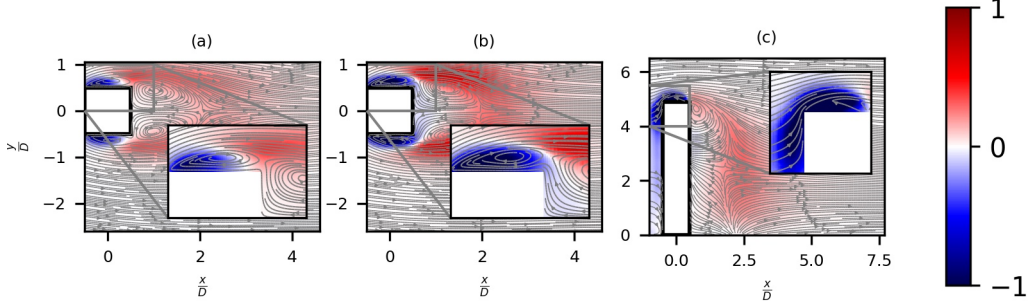


Figure 25: Converged parameter  $f_\epsilon$ , with projection in  $H^1$  ( $l_{sob} = 0.1D$ ); (a), at horizontal plan at  $z/H_{ref} = 0.19$ , (b)  $z/H_{ref} = 1$  and, (c) at symmetry plan  $y/D = 0$ .

## 933 6. Conclusions

934 The use of steady RANS models under the eddy viscosity hypothesis is known to be inaccurate  
 935 for practical applications such as micro-climate studies (at urban scale). For instance, in the  
 936 prediction of wind-loads on a high-rise building, most of state-of-the-art  $k - \epsilon$  turbulence  
 937 models (including the realizable revision studied here) tend to give poor wake flow accuracy  
 938 estimations, as well as an inaccurate wall-pressure value, when compared to wind tunnel  
 939 experiments. One way to tackle this deficiency consists in adopting data-model coupling  
 940 techniques such as the variational DA approach based on optimal control. To set up such a  
 941 framework in our context we devised a consistent analytical derivation of one of the most  
 942 common turbulence models (*i.e.* realizable revision of  $k - \epsilon$ ) coupled with near wall closure.  
 943 This has resulted in the definition of a continuous adjoint model (together with its consistent  
 944 boundary conditions) of the tangent linear operator of the RANS model. Given the dual  
 945 description of the dynamics composed of the RANS direct model and the adjoint of its  
 946 tangent linear representation, we have explored three methodological settings that provides  
 947 an efficient sensitivity analysis and an in-depth diagnosis of the turbulence closure adopted  
 948 on such flows.

949 The first tool consisted in the inspection of the adjoint state variables in relation with their  
 950 physical meaning. The second one was dedicated to providing a better understanding of the  
 951 model output's variabilities in terms of the model's closure global constants. With the last  
 952 one, we went one step further. We considered the adjunction of a distributed parameter which  
 953 enables the reanalysis of the closure at a structural level (such as the choice of the transport  
 954 equation for the energy dissipation rate on the  $k - \epsilon$  model as considered here). To conduct  
 955 an efficient structural inspection, a distributed parameter is sought in a Sobolev space and  
 956 further estimated through a data-assimilation procedure. As a sensitivity field is generally  
 957 not very regular for distributed parameters, a projection onto the Sobolev space  $H^1(\Omega)$  was  
 958 proposed here for both a regularisation purpose and to define an improved descent direction  
 959 for the minimising technique. These three settings have then been applied to a high-rise  
 960 building case study.

961 Sensitivity maps of the  $k - \epsilon$  global coefficients had revealed high interest in optimising  
 962 them mainly at the shear layers resulting from flow separations at the leading lateral edges and  
 963 on top of the building. Moreover, little sensitivity in the bulk of the recirculation wake region  
 964 was observed. Despite all the spatial variability of the sensitivity fields, it was shown that  
 965 the optimality condition drastically reduces the high dimensional dependency of the model  
 966 to each coefficient. Regarding the model hypotheses which guided the choice for closed  
 967 default values, a better data coupling is obtained by enforcing the constraint that equates  
 968 turbulence energy mixing to momentum mixing, even if it offers fewer degrees of freedom in

969 the optimisation. This suggests that it is a physically valid hypothesis that structures the model  
970 and then helps for convergence. Conversely, by relaxing this constraint and establishing the  
971 relation (5.1), which dictates a strong bound limiting the production of energy dissipation  
972 rate to its redistribution (supposedly valid in the inertial layer near the wall), this leads to  
973 lower agreement with experiments. As both assumptions constitute a common practice for  
974 closure to most eddy viscosity models, it is expected that these results extend to several  
975 other models of similar forms. The limited performance of the DA procedure, achieved when  
976 controlling global turbulence parameters, points out the rigidity of the considered turbulence  
977 model when used with realistic wall pressure measurements.

978 Considering a distributed parameter to the  $\epsilon$  budget, in order to complement the model in  
979 terms of local source/sink process, sensitivity maps highlight regions where global constants  
980 are not too sensitive (for instance, the wake region) and exhibit relatively less variability in  
981 term of sign changes. Maps had actually revealed binary tendencies, separating the lateral  
982 and top shear regions and the wake flow. Regarding the regularisation, a comparison of the  
983 cost reduction results with a conventional penalisation approach showed that projection in  
984  $H^1(\Omega)$  yields a much faster convergence and lower discrepancy levels. Let us note that, along  
985 with the  $H^1(\Omega)$  projection, the robustness of the DA procedure was enabled as a first order  
986 numerical scheme to solve the dual dynamics. Regarding the reconstruction ability, compared  
987 with coefficient calibration, the modified closure model produced better results in most of the  
988 building's wall regions in terms of wind load profiles, yet, results suggest some remaining  
989 restrictions as reconstructed profiles tend toward the original model in some regions. An  
990 excellent agreement with PIV experiments was obtained in wake transverse extension. It  
991 should be recalled that only pressure measurements in the facade have been assimilated.  
992 This good agreement with measurements of different nature and that have not been used in  
993 the assimilation proved that we are neither overfitting the data nor in an over-constrained  
994 situation.

995 This work thus illustrates the capabilities of adjoint methods. Beyond providing a data-  
996 driven flow reconstruction, they enable an in-depth analysis of the turbulence closure. Indeed,  
997 by regarding adjoint fields as a physical forcing, rather than as a purely mathematical object,  
998 these data-driven reconstructed fields allows to highlight a misrepresentation of the turbulent  
999 flow by the RANS model, and hence, to address errors within a particular turbulence  
1000 modelling form (*e.g.* energy production, backscattering, redistribution or dissipation).  
1001 Although the results presented were for a particular turbulence model and on a specific  
1002 bluff-body-like case, over-estimation of the recirculation length in bluff bodies is a common  
1003 features in RANS models, and the proposed methodology could be employed without loss  
1004 of generality. Provided sparse wall pressure measurements, the technique can be directly  
1005 applied to any complex wake flow embedded in the atmospheric boundary layer.

## 1006 **Acknowledgements**

1007 This work was supported by the Centre Scientifique et Technique du Bâtiment (CSTB)  
1008 (Nantes, France) in collaboration with mixed research team Fluminance (INRIA, INRAE  
1009 in Rennes, France). The authors wish to deeply thank Fabrice De Oliveira, for his help in  
1010 providing us the experimental data.

## 1011 **Declaration of Interests**

1012 The authors report no conflict of interest.

1013 **APPENDIX**

1014 Under differentiability condition, it can be shown (Le Dimet & Talagrand 1986; Gunzburger  
1015 2003) that the problem of determining the optimal set of flow state variables,

$$1016 \quad \mathbf{X} = (U_x, U_y, U_z, P, k, \epsilon, \mu_t)$$

1017 and the set of parameters  $\alpha$ , of the cost function  $\mathcal{J}(\mathbf{X}, \alpha)$  under the constraint

$$1018 \quad \mathbf{M}(\mathbf{X}, \alpha) = 0$$

1019 is equivalent to the problem of determining the optimal set of these variables in addition to  
1020 an adjoint state

$$1021 \quad \mathbf{X}^* = (U_x^*, U_y^*, U_z^*, P^*, k^*, \epsilon^*, \mu_t^*)$$

of the Lagrangian functional  $\mathcal{L}(\mathbf{X}, \mathbf{X}^*, \alpha)$ . With the inner product defined as  $\langle \psi, \phi \rangle_\Omega = \int_\Omega \psi^T \phi \, d\Omega$  where  $\psi$  and  $\phi$  are any two regular vectorial functions defined on the domain  $\Omega$ , the Lagrangian, is

$$\mathcal{L}(\mathbf{X}, \mathbf{X}^*, \alpha) = \mathcal{J}(P, \alpha) + \int_\Omega (\mathbf{X}^*)^T \mathbf{M}(\mathbf{X}, \alpha) \, d\Omega.$$

1022 The first order variation  $\delta \mathcal{L}$  resulting from perturbation  $(\delta \mathbf{X}, \delta \mathbf{X}^*, \delta \alpha)$  of  $(\mathbf{X}, \mathbf{X}^*, \alpha)$ , in  
1023 compact form, is equal to

$$\begin{aligned} 1024 \quad \delta \mathcal{L} &= \frac{\partial \mathcal{J}}{\partial P} \delta P + \frac{\partial \mathcal{J}}{\partial \alpha} \delta \alpha + \int_\Omega (\mathbf{X}^*)^T \left( \frac{\partial \mathbf{M}}{\partial U_x} \delta U_x \right) \, d\Omega + \int_\Omega (\mathbf{X}^*)^T \left( \frac{\partial \mathbf{M}}{\partial U_y} \delta U_y \right) \, d\Omega \\ 1025 \quad &+ \int_\Omega (\mathbf{X}^*)^T \left( \frac{\partial \mathbf{M}}{\partial U_z} \delta U_z \right) \, d\Omega + \int_\Omega (\mathbf{X}^*)^T \left( \frac{\partial \mathbf{M}}{\partial P} \delta P \right) \, d\Omega + \int_\Omega (\mathbf{X}^*)^T \left( \frac{\partial \mathbf{M}}{\partial k} \delta k \right) \, d\Omega \\ 1026 \quad &+ \int_\Omega (\mathbf{X}^*)^T \left( \frac{\partial \mathbf{M}}{\partial \epsilon} \delta \epsilon \right) \, d\Omega + \int_\Omega (\mathbf{X}^*)^T \left( \frac{\partial \mathbf{M}}{\partial \mu_t} \delta \mu_t \right) \, d\Omega + \int_\Omega (\delta \mathbf{X}^*)^T \mathbf{M}(\mathbf{X}, \alpha) \, d\Omega. \quad (6.1) \\ 1027 \end{aligned}$$

1028 Using the duality identity defined as

$$1029 \quad \int_\Omega (\mathbf{L}\phi) \psi \, d\Omega = \int_{\partial\Omega} (\mathbf{B}\phi) (\mathbf{C}\psi) \, d\partial\Omega - \int_\Omega \phi (\mathbf{L}^* \psi) \, d\Omega$$

where  $\mathbf{L}$  is a linear differential operator and  $(\mathbf{B}, \mathbf{C})$  are lower order differential operators, resulting from the integration by part, that embed the natural boundary condition,  $\delta \mathcal{L}$  becomes

$$\begin{aligned} \delta \mathcal{L} &= \frac{\partial \mathcal{J}}{\partial P} \delta P + \frac{\partial \mathcal{J}}{\partial \alpha} \delta \alpha - \int_\Omega \left( \frac{\partial \mathbf{M}^*}{\partial U_x} \mathbf{X}^* \right)^T \delta U_x \, d\Omega - \int_\Omega \left( \frac{\partial \mathbf{M}^*}{\partial U_y} \mathbf{X}^* \right)^T \delta U_y \, d\Omega \\ &- \int_\Omega \left( \frac{\partial \mathbf{M}^*}{\partial U_z} \mathbf{X}^* \right)^T \delta U_z \, d\Omega - \int_\Omega \left( \frac{\partial \mathbf{M}^*}{\partial P} \mathbf{X}^* \right)^T \delta P \, d\Omega - \int_\Omega \left( \frac{\partial \mathbf{M}^*}{\partial k} \mathbf{X}^* \right)^T \delta k \, d\Omega \\ &- \int_\Omega \left( \frac{\partial \mathbf{M}^*}{\partial \epsilon} \mathbf{X}^* \right)^T \delta \epsilon \, d\Omega - \int_\Omega \left( \frac{\partial \mathbf{M}^*}{\partial \mu_t} \mathbf{X}^* \right)^T \delta \mu_t \, d\Omega + \int_\Omega (\delta \mathbf{X}^*)^T \mathbf{M}(\mathbf{X}, \alpha) \, d\Omega \\ &\quad + \int_{\partial\Omega} (\delta \mathbf{X})^T (\mathbf{C}\mathbf{X}^*) \, d\partial\Omega + \int_{\partial\Omega} (\mathbf{B}\delta \mathbf{X})^T \mathbf{X}^* \, d\partial\Omega. \end{aligned}$$

Since the perturbations are arbitrary, setting the first variation of  $\mathcal{L}$  with respect to the Lagrangian arguments equal to zero leads to an optimality system. With respect to an arbitrary variation of the adjoint state, we recover the constraint equations; while for an arbitrary variation of the state  $\mathbf{X}$  all the terms that include the product of adjoint state to the

tangent linear of the constraint has to vanish. Further, with respect to the set of parameters, vanishing the total variation leads to an optimality condition that enclose the optimality system. Collecting these results yields to

$$\begin{aligned}
 \text{state equations} &\Rightarrow \mathbf{M}(\mathbf{X}, \alpha) = 0 \\
 \text{adjoint equations} &\Rightarrow \left( \frac{\partial \mathbf{M}}{\partial \mathbf{X}} \right)^* \mathbf{X}^* = 0 \\
 \text{optimality condition} &\Rightarrow \frac{\partial \mathcal{J}}{\partial \alpha} + \left( \frac{\partial \mathbf{M}}{\partial \alpha} \right)^* \mathbf{X}^* = 0,
 \end{aligned}$$

1030 where  $\left( \frac{\partial \mathbf{M}}{\partial \alpha} \right)^*$  is the adjoint of the model derivative with respect to the parameters. If it is  
 1031 possible to solve this coupled optimality system through one-shot methods, then optimal  
 1032 states and parameters can be obtained without an optimisation iteration. However, due to  
 1033 non linearity and the very large size of this system ( $\sim 3 \times \text{size}(\mathbf{X})$ ) one still have to iterate  
 1034 in order to solve the optionality system. Thus, having solved the state equations for  $\mathbf{X}$  and  
 1035 then  $\mathbf{X}^*$  solution of the adjoint system, model parameters can be iterated by a gradient based  
 1036 optimisation algorithm until optimality condition is satisfied. In a steepest descent algorithm,  
 1037 the parameter is updated at an iteration  $n$  according to:

~~1038~~

$$\alpha^{n+1} = \alpha^n - \lambda_n d_n \quad (6.2)$$

1040 where  $d_n$  is the descent direction which is defined recursively by:

$$d_n = \frac{\partial \mathcal{L}}{\partial \alpha} = \left( \frac{\partial \mathbf{M}}{\partial \alpha} \right)^* \mathbf{X}^* + \frac{\partial \mathcal{J}}{\partial \alpha}, \quad (6.3)$$

1042 Concerning adjoint based optimisation methods, we refer the reader to (Gunzburger 2003;  
 1043 Gronsksis *et al.* 2013).

## REFERENCES

- 1044 BRYSON, ARTHUR EARL 1975 *Applied optimal control: optimization, estimation and control*. CRC Press.
- 1045 CERMAK, JACK E & KOLOSEUS, HERMAN J 1954 Development of a miniature air velocity indicator:  
 1046 experimental study to determine sensitivity of new designs. *CER*; 54-23 .
- 1047 CHANDRAMOULI, PRANAV, MEMIN, ETIENNE & HEITZ, DOMINIQUE 2020 4D large scale variational data  
 1048 assimilation of a turbulent flow with a dynamics error model. *Journal of Computational Physics* p.  
 1049 109446.
- 1050 COCHRAN, LEIGHTON & DERICKSON, RUSS 2011 A physical modeler's view of computational wind  
 1051 engineering. *Journal of Wind Engineering and Industrial Aerodynamics* **99** (4), 139–153.
- 1052 DUYNKERKE, PG 1988 Application of the  $E-\epsilon$  turbulence closure model to the neutral and stable atmospheric  
 1053 boundary layer. *Journal of the Atmospheric Sciences* **45** (5), 865–880.
- 1054 EDELING, WN, CINNELLA, PASQUALE, DWIGHT, RICHARD P & BIJL, HESTER 2014 Bayesian estimates of  
 1055 parameter variability in the  $k-\epsilon$  turbulence model. *Journal of Computational Physics* **258**, 73–94.
- 1056 EN, NF 2005 1-4: Eurocode 1: Actions sur les structures–partie 1-4: Actions générales–actions du vent.
- 1057 ERRICO, RONALD M 1997 What is an adjoint model? *Bulletin of the American Meteorological Society* **78** (11),  
 1058 2577–2592.
- 1059 ETLING, D, DETERING, HW & THEUNERT, F 1985 On the simulation of wind-driven currents in shallow  
 1060 water. *Archives for meteorology, geophysics, and bioclimatology, Series A* **33** (4), 355–363.
- 1061 FOURES, DIMITRY PG, DOVETTA, NICOLAS, SIPP, DENIS & SCHMID, PETER J 2014 A data-assimilation method  
 1062 for Reynolds-Averaged Navier-Stokes-driven mean flow reconstruction. *Journal of Fluid Mechanics*  
 1063 **759**, 404–431.
- 1064 FRANCESCINI, LUCAS, SIPP, DENIS & MARQUET, OLIVIER 2020 Mean-flow data assimilation based on  
 1065 minimal correction of turbulence models: Application to turbulent high reynolds number backward-  
 1066 facing step. *Phys. Rev. Fluids* **5**, 094603.

- 1067 GILES, MICHAEL B & PIERCE, NILES A 2000 An introduction to the adjoint approach to design. *Flow,*  
1068 *Turbulence and Combustion* **65** (3-4), 393–415.
- 1069 GRONSKIS, ALEJANDRO, HEITZ, DOMINIQUE & MÉMIN, ETIENNE 2013 Inflow and initial conditions for direct  
1070 numerical simulation based on adjoint data assimilation. *Journal of Computational Physics* **242**,  
1071 480–497.
- 1072 GUNZBURGER, MAX D 2003 *Perspectives in flow control and optimization*, , vol. 5. SIAM.
- 1073 HALL, MATTHEW CG & CACUCI, DAN G 1983 Physical interpretation of the adjoint functions for sensitivity  
1074 analysis of atmospheric models. *Journal of the Atmospheric Sciences* **40** (10), 2537–2546.
- 1075 IRWIN, PETER A & KOCHANSKI, WILL W 1995 Measurement of structural wind loads using the high frequency  
1076 pressure integration method. In *Restructuring: America and Beyond*, pp. 1631–1634. ASCE.
- 1077 JASAK, H 1996 Error analysis and estimation in the finite volume method with applications to fluid flows.  
1078 PhD thesis, Imperial College, University of London. 1028.
- 1079 JENSEN, MARTIN 1958 The model-law for phenomena in natural wind. *Ingenioren* **2** (2), 121–128.
- 1080 KAWAMURA, TAKAO, HIWADA, MUNEHIKO, HIBINO, TOSHIHARU, MABUCHI, IKUO & KUMADA, MASAYA 1984  
1081 Flow around a finite circular cylinder on a flat plate: Cylinder height greater than turbulent boundary  
1082 layer thickness. *Bulletin of JSME* **27** (232), 2142–2151.
- 1083 LAUNDER, BRIAN EDWARD & SHARMA, BI 1974 Application of the energy-dissipation model of turbulence  
1084 to the calculation of flow near a spinning disc. *Letters in Heat and Mass Transfer* **1** (2), 131–137.
- 1085 LE DIMET, FRANÇOIS-XAVIER & TALAGRAND, OLIVIER 1986 Variational algorithms for analysis and  
1086 assimilation of meteorological observations: theoretical aspects. *Tellus A: Dynamic Meteorology*  
1087 *and Oceanography* **38** (2), 97–110.
- 1088 LI, YI, ZHANG, JIANLEI, DONG, GANG & ABDULLAH, NASEER S 2020 Small-scale reconstruction in three-  
1089 dimensional Kolmogorov flows using four-dimensional variational data assimilation. *Journal of Fluid*  
1090 *Mechanics* **885**.
- 1091 LI, ZHIYONG, ZHANG, HUAIBAO, BAILEY, SEAN CC, HOAGG, JESSE B & MARTIN, ALEXANDRE 2017 A  
1092 data-driven adaptive Reynolds-Averaged Navier–Stokes  $k - \omega$  model for turbulent flow. *Journal of*  
1093 *Computational Physics* **345**, 111–131.
- 1094 MARGHERI, LUCA, MELDI, MARCELLO, SALVETTI, MARIA VITTORIA & SAGAUT, PIERRE 2014 Epistemic  
1095 uncertainties in rans model free coefficients. *Computers & Fluids* **102**, 315–335.
- 1096 MELDI, MARCELLO & POUX, ALEXANDRE 2017 A reduced order model based on Kalman filtering for  
1097 sequential data assimilation of turbulent flows. *Journal of Computational Physics* **347**, 207–234.
- 1098 MERONEY, ROBERT N & DERICKSON, RUSS 2014 Virtual reality in wind engineering: the windy world within  
1099 the computer. *Journal of Wind Engineering and Industrial Aerodynamics* **11** (2), 11–26.
- 1100 MONS, VINCENT, CHASSAING, J-C, GOMEZ, THOMAS & SAGAUT, PIERRE 2016 Reconstruction of unsteady  
1101 viscous flows using data assimilation schemes. *Journal of Computational Physics* **316**, 255–280.
- 1102 MONS, V, MARGHERI, LUCA, CHASSAING, J-C & SAGAUT, PIERRE 2017 Data assimilation-based reconstruction  
1103 of urban pollutant release characteristics. *Journal of Wind Engineering and Industrial Aerodynamics*  
1104 **169**, 232–250.
- 1105 MOUKALLED, FADL, MANGANI, L & DARWISH, MARWAN 2016 *The finite volume method in computational*  
1106 *fluid dynamics*, , vol. 113. Springer.
- 1107 MURAKAMI, SHUZO 1990 Computational wind engineering. *Journal of Wind Engineering and Industrial*  
1108 *Aerodynamics* **36**, 517–538.
- 1109 MURAKAMI, SHUZO 1997 Current status and future trends in computational wind engineering. *Journal of*  
1110 *Wind Engineering and Industrial Aerodynamics* **67**, 3–34.
- 1111 OTHMER, C 2008 A continuous adjoint formulation for the computation of topological and surface  
1112 sensitivities of ducted flows. *International Journal for Numerical Methods in Fluids* **58** (8), 861–877.
- 1113 PLESSIX, R-E 2006 A review of the adjoint-state method for computing the gradient of a functional with  
1114 geophysical applications. *Geophysical Journal International* **167** (2), 495–503.
- 1115 POPE, STEPHEN B 2001 Turbulent flows.
- 1116 PROTAS, BARTOSZ, BEWLEY, THOMAS R & HAGEN, GREG 2004 A computational framework for the  
1117 regularization of adjoint analysis in multiscale pde systems. *Journal of Computational Physics*  
1118 **195** (1), 49–89.
- 1119 RHIE, CM & CHOW, W LI 1983 Numerical study of the turbulent flow past an airfoil with trailing edge  
1120 separation. *AIAA journal* **21** (11), 1525–1532.
- 1121 RICHARDS, PJ & HOXEY, RP 1993 Appropriate boundary conditions for computational wind engineering  
1122 models using the  $k - \epsilon$  turbulence model. In *Computational Wind Engineering*, pp. 145–153. Elsevier.
- 1123 SHENG, R, PERRET, L, CALMET, I, DEMOUGE, F & GUILHOT, J 2018 Wind tunnel study of wind effects on a



- 1124 high-rise building at a scale of 1: 300. *Journal of Wind Engineering and Industrial Aerodynamics*  
1125 **174**, 391–403.
- 1126 SHIH, TSAN-HSING, LIOU, WILLIAM W, SHABIR, AAMIR, YANG, ZHIGANG & ZHU, JIANG 1995 A new  $k - \epsilon$   
1127 eddy viscosity model for high Reynolds number turbulent flows-model development and validation.  
1128 Document ID: 19950005029 (Acquired Dec 28, 1995) Accession (95N11442).
- 1129 SHIRZADI, MOHAMMADREZA, MIRZAEI, PARHAM A & NAGHASHZADEGAN, MOHAMMAD 2017 Improvement  
1130 of k-epsilon turbulence model for CFD simulation of atmospheric boundary layer around a high-  
1131 rise building using stochastic optimization and Monte-Carlo sampling technique. *Journal of Wind*  
1132 *Engineering and Industrial Aerodynamics* **171**, 366–379.
- 1133 SINGH, ANAND PRATAP & DURAISAMY, KARTHIK 2016 Using field inversion to quantify functional errors in  
1134 turbulence closures. *Physics of Fluids* **28** (4), 045110.
- 1135 SURRY, D 1999 Wind loads on low-rise buildings: Past, present and future. *Wind Engineering into the 21<sup>st</sup>*  
1136 *Century*.
- 1137 SYMON, SEAN, DOVETTA, NICOLAS, McKEON, BEVERLEY J, SIPP, DENIS & SCHMID, PETER J 2017 Data  
1138 assimilation of mean velocity from 2D PIV measurements of flow over an idealized airfoil.  
1139 *Experiments in Fluids* **58** (5), 61.
- 1140 TAVOULARIS, S & KARNIK, U 1989 Further experiments on the evolution of turbulent stresses and scales in  
1141 uniformly sheared turbulence. *Journal of Fluid Mechanics* **204**, 457–478.
- 1142 TISSOT, GILLES, BILLARD, ROBIN & GABARD, GWENael 2020 Optimal cavity shape design for acoustic liners  
1143 using helmholtz equation with visco-thermal losses. *Journal of Computational Physics* **402**, 109048.
- 1144 TOMINAGA, YOSHIHIDE, MOCHIDA, AKASHI, YOSHIE, RYUICHIRO, KATAOKA, HIROTO, NOZU, TSUYOSHI,  
1145 YOSHIKAWA, MASARU & SHIRASAWA, TAICHI 2008 AIJ guidelines for practical applications of cfd  
1146 to pedestrian wind environment around buildings. *Journal of Wind Engineering and Industrial*  
1147 *Aerodynamics* **96** (10-11), 1749–1761.
- 1148 TOMINAGA, YOSHIHIDE & STATHOPOULOS, TED 2010 Numerical simulation of dispersion around an isolated  
1149 cubic building: model evaluation of RANS and LES. *Building and Environment* **45** (10), 2231–2239.
- 1150 TOMINAGA, YOSHIHIDE & STATHOPOULOS, TED 2017 Steady and unsteady RANS simulations of pollutant  
1151 dispersion around isolated cubical buildings: Effect of large-scale fluctuations on the concentration  
1152 field. *Journal of Wind Engineering and Industrial Aerodynamics* **165**, 23–33.
- 1153 TSCHANZ, T & DAVENPORT, ALAN GARNETT 1983 The base balance technique for the determination of  
1154 dynamic wind loads. *Journal of Wind Engineering and Industrial Aerodynamics* **13** (1-3), 429–439.
- 1155 TSUCHIYA, M, MURAKAMI, S, MOCHIDA, A, KONDO, K & ISHIDA, Y 1997 Development of a new  $k - \epsilon$   
1156 model for flow and pressure fields around bluff body. *Journal of Wind Engineering and Industrial*  
1157 *Aerodynamics* **67**, 169–182.
- 1158 VERSTEEG, HENK KAARLE & MALALASEKERA, WEERATUNGE 2007 *An introduction to computational fluid*  
1159 *dynamics: the finite volume method*. Pearson education.
- 1160 WANG, HF & ZHOU, YU 2009 The finite-length square cylinder near wake. *Journal of Fluid Mechanics* **638**,  
1161 453–490.
- 1162 YAKHOT, VSASTBCG, ORSZAG, SA, THANGAM, SIVA, GATSKI, TB & SPEZIALE, CG 1992 Development  
1163 of turbulence models for shear flows by a double expansion technique. *Physics of Fluids A: Fluid*  
1164 *Dynamics* **4** (7), 1510–1520.
- 1165 YANG, YIN, ROBINSON, CORDELIA, HEITZ, DOMINIQUE & MÉMIN, ETIENNE 2015 Enhanced ensemble-based  
1166 4d-var scheme for data assimilation. *Computers & Fluids* **115**, 201–210.
- 1167 YOSHIE, R, MOCHIDA, A, TOMINAGA, Y, KATAOKA, H, HARIMOTO, K, NOZU, T & SHIRASAWA, T 2007  
1168 Cooperative project for CFD prediction of pedestrian wind environment in the architectural institute  
1169 of Japan. *Journal of Wind Engineering and Industrial Aerodynamics* **95** (9-11), 1551–1578.
- 1170 ZYMARIS, AS, PAPANIMITRIOU, DI, GIANNAKOGLOU, KYRIAKOS C & OTHMER, C 2010 Adjoint wall functions:  
1171 A new concept for use in aerodynamic shape optimization. *Journal of Computational Physics*  
1172 **229** (13), 5228–5245.